

**AN EXPERIMENTAL STUDY ON JET IMPINGEMENT
ON A VERY HIGH SPEED MOVING SURFACE**

by

GEORGE EARL GRANT STERLING

B.A.S.c., The University of British Columbia, 2010

**A THESIS SUBMITTED IN PARTIAL FILFILLMENT OF
THE REQUIREMENTS FOR THE DEGREE OF
MASTER OF APPLIED SCIENCE**

in

THE FACULTY OF GRADUATE STUDIES

(Mechanical Engineering)

THE UNIVERSITY OF BRITISH COLUMBIA

(Vancouver)

August 2012

© George Earl Grant Sterling, 2012

Abstract

Motivated by the need to improve transfer efficiencies of liquid coatings from jet impingement, an experimental investigation into jet impingement on very high speed moving surfaces is presented. Seven different Newtonian liquids with widely varying shear viscosities were made to impinge on a surface which could be made to move at speeds up to 350km/hr. Tests for the Newtonian liquids were done with several modified surfaces to study the effects of roughness and surface inconsistencies. Nozzle sizes and impingement angles were varied to interrogate their effects on the interaction of the impacting jet and moving surface while high speed photography was employed to capture these interactions. Spread radii and spread widths were measured for viscous fluids which deposited.

While it was observed that stable jets of fluids with sufficiently high viscosities almost always deposited, tests with water indicate that the effects of the impingement angle as well as jet diameter significantly alter the locations of boundaries between deposition, spatter and lamella lift-off. Impingement angles that result in jet velocities with large components of velocity parallel to the surface velocity are prone to deposit. Jets of smaller diameters are also prone to deposit. It was observed that both the jet velocity and surface velocity are important determining factors in the likelihood of deposition.

The deposition of viscous fluids demonstrated that it is possible to observe transitions from deposition to lift-off and vice versa through mechanisms that trigger random fluctuations in the lamella. The track distance covered before a transition from lift-off to deposition occurs is shown to be a Poisson Process.

Table of Contents

Abstract	ii
Table of Contents	iii
List of Tables	v
List of Figures	vi
List of Equations	viii
List of Symbols	ix
Acknowledgements	x
1 Introduction	1
1.1. Friction Control in the Rail Road Industry	1
1.2. Droplet Impaction	1
1.3. Liquid Jet Impingement	2
1.4. Research Objectives	3
2 Mass Flow Rates	4
3 Water Tests	7
4 Water-Glycerin Tests	12
5 Triggering and Recovery	17
6 Repeatability Tests	21
7 Conclusions and Recommendations for Future Work	24
7.1. Conclusions for Water Tests	24
7.2. Conclusions for Water-Glycerin Tests	24
7.3. Recommendations for Future Work	25
Bibliography	26
Appendices	28
Appendix A: Equipment and Usage	28
A.1. Device Summary	28
A.2. The Disk	30
A.3. Safety Enclosure	31
A.4. Nozzle Assembly	32
A.5. Imaging	35
A.6. Auto-Pressure Controller	37
A.7. Control Box	38
A.8. Software	38
A.9. Motor Control	40
Appendix B: Schematics	41

Appendix C: Supplementary Data.....42

List of Tables

Table 2.1 The Composition and properties of Newtonian test liquids at 25 C.....	5
Table 2.2 Empirical Fit Parameters	6
Table 3.1 Water Test Legend	9
Table 6.1 Experimental configuration values and resulting curve fit data	23
Table C.1 Fitted lines (Varied V_s , V_j).....	47
Table C.2 Fitted lines (Varied d , V_j).....	48
Table C.3 Fitted lines (Varied ψ , V_j).....	49

List of Figures

Figure 2.1 Calculated Jet Speed from MFR	5
Figure 3.1 Schematic of Impingement	7
Figure 3.2 Figure 3.2 Three Categories of Impingement.....	8
Figure 3.3 Results of Water Impingement	9
Figure 3.4 Extracted Boundary Information	10
Figure 4.1 Deposition of 73%g.w. for $V_s=96\text{m/s}$, $V_j=15\text{m/s}$ $\phi=90^\circ$, $d=800\mu\text{m}$	12
Figure 4.2 Spread Width and Spread Length Schematic	13
Figure 4.3 Radius vs Width of 73%g.w. for $V_s=32\text{m/s}$, $V_j=\text{varied}$ $\phi=\text{varied}$, $d=800\mu\text{m}$	14
Figure 4.4 Non-dimensional data (Radius)	14
Figure 4.5 Non-dimensional data (Width).....	145
Figure 5.1 Oncoming view of impingement of a jet from an $800\mu\text{m}$ orifice oriented at $\phi= 60^\circ$	17
Figure 5.2 Top view and side view of recovery of a jet from an $800\mu\text{m}$ orifice oriented at $\phi= 60^\circ$	18
Figure 5.3 Intentional Surface Discontinuity	19
Figure 5.4 Intentional Surface Roughness	20
Figure 6.1 Recovery probability vs Track partitions (Left to Right).....	22
Figure A.1 Schematic of apparatus	29
Figure A.2 Photograph of actual apparatus	29
Figure A.3 Balanced disk.....	31
Figure A.4 Surface polish	31
Figure A.5 Nozzle block.....	33
Figure A.6 Nozzle assembly	33
Figure A.7 Nozzle orifice pucks	34
Figure A.8 Measured orifice diameters.....	34
Figure A.9 Measured orifice diameters and residuals	35
Figure A.10 High intensity LED light without collimating lens.....	36
Figure A.11 Two camera angles.....	36
Figure A.12 Auto-pressure controller.....	37
Figure A.13 Control box	38
Figure A.14 Control software	40
Figure A.15 Motor control pane	41
Figure B.1 Relay circuits.....	41
Figure B.2 H-bridge circuit.....	42
Figure C.1 35° water impingement results	42
Figure C.2 60° water impingement results	43

Figure C.3 90° water impingement results	44
Figure C.4 135° water impingement results	45
Figure C.5 160° water impingement results	46
Figure C.6 73% g.w. lamella dimensions (Varied V_s , V_j)	47
Figure C.7 73% g.w. lamella dimensions (Varied d , V_j)	48
Figure C.8 73% g.w. lamella dimensions (Varied ψ , V_j).....	49

List of Equations

Equation 2.1..... 4
Equation 2.2..... 4
Equation 2.3..... 4
Equation 2.4..... 6
Equation 4.1..... 13
Equation 4.2..... 13
Equation 4.3..... 13
Equation 6.1..... 21
Equation 6.2..... 21
Equation 6.3..... 21
Equation 6.4..... 21
Equation 6.5..... 22
Equation 6.6..... 22
Equation 6.7..... 22

List of Symbols

μ	Dynamic viscosity [Pa.s]
ρ	Fluid density [Kg.m ⁻³]
ν	Kinematic viscosity [m ² .s ⁻¹]
φ	Impingement angle [Degrees]
V_s	Surface speed [m.s ⁻¹]
V_j	Jet speed [m.s ⁻¹]
ω	Angular rate of disk [rpm]
$V_{ }$	Parallel component of velocity [m.s ⁻¹]
V_{\perp}	Perpendicular component of velocity [m.s ⁻¹]
R_p	Spread radius measured in pixels [pixels]
W_p	Spread width measured in pixels [pixels]
W	Spread width [m]
R	Spread radius [m]
δq_i	Error in variable q_i
d_o	Orifice Diameter [μ m]
d	Jet diameter [μ m]
Re	Reynolds number
D_s	Partitioned Track Length
E_f	Event of a random fluctuation
E_r	Event of recovery
X_N	Random counting variable
λ	Rate parameter
p	Probability of E_i and R happening
Y_{D_s}	Random counting variable
r^2	Correlation Coefficient
g	Glycerin percentage by weight [%]
w	Water percentage by weight [%]

Acknowledgements

I wish to thank my supervisor Sheldon Green for his exemplary mentorship during the past two years. It was an honor and a pleasure to work with you. Your unending guidance not only efficiently directed the course of the project, but gained me maturity in other categories that will inevitably advance me further in my career.

Many thanks go to our sponsors. Without the financial assistance from Kelsan and the National Sciences and Engineering Research Council of Canada this project would not have been possible.

I wish extended thanks towards Don Eadie, Dave Elvidge, and John Cotter from Kelsan for their technical advice throughout this project and for their continued attention to detail and insightful comments at our meetings. This meticulous research attitude has, short from anything else, inspired me.

The work and help of co-op students Arnaud Galley and Coralie Pompeu are appreciated.

I wish to thank Markus Fengler for his expert insight and opinions on many of my initial designs. It is unknown the amount of time and frustration you have saved me in recommending alternate paths to a solution; though, the savings were likely much greater than the time and frustrations involved with the suggested re-designs.

1 Introduction

1.1. Friction Control in the Rail Road Industry

Rail transport is still one of the most efficient and cost-effective forms of freight and passenger transportation and will continue to be due to the demands for transportation from growing populations. Rising fuel costs ensure that alternative methods such as truck and air transport are financially less desirable options.

It is recognized that through effectively managing the wheel-rail interface railways can see additional fuel saving as well as reduced rail and wheel wear rates ^[1]. Research has progressed with top of rail (TOR) friction control which is shown to significantly reduce fuel consumption, lateral (curving forces), and wheel/rail wear rates ^[2].

Kelsan Technologies Corporation is a leader in developing friction modifiers (FM) for the railway industry and has developed many specialized FMs for various applications. Currently much research is devoted to the development of highly effective application methods for their liquid friction modifiers (LFMs), made up of a water-based suspension of polymers and inorganic solids ^[3]. Due to the compositional nature of these FMs, non-Newtonian behavior is inherently exhibited.

The current method of application is via air-blast atomization which ejects small droplets from a nozzle. The transfer efficiency is poor due to the non-uniformity of droplet shape and size as well as large deflections resulting from crosswinds typically present underneath train cars ^[1,4,5].

1.2. Droplet Impaction

The interaction of liquid droplets on surfaces has received much attention as a topic of study due to a plethora of technical applications stemming from the deposition of solder to printed circuit boards ^[8] for electronics industries to pesticide applications and the dispersal of fungal spores by raindrop splashing ^[7] for agricultural industries to fuel injection for automotive and gas turbine industries. It is shown that the results of droplet impaction stationary surfaces can be categorized in a total of six categories, namely,

deposition, prompt splash, corona splash, receding breakup, partial rebound, and complete rebound ^[9]. These six categories fit into two primary categories, namely, deposition and splash. Rioboo et al. ^[9] show that in the later stages of the impaction phenomena, the outcome is dependent upon the droplet diameter, impingement velocity and the fluid and surface properties. When a moving surface is introduced it is found that the tangential surface velocity is also an important determining parameter in the resulting categorization ^[6, 10, 12]. In some cases the tangential velocity results in a boundary layer that entirely lifts the droplet from the surface ^[11]. Additionally, Bird et al. ^[14] observe asymmetric splashing as a result of the surface velocity.

1.3. Liquid Jet Impingement

In contrast to the extensive research done in droplet impaction on moving surfaces, few have studied liquid jet impingement on high speed moving surfaces. Much of what currently exists is in the area of heat transfer and reveals little about transfer efficiencies. It hasn't been until very recently that splash and deposition criteria have been studied. Some authors describe the interactions of non-circular jets with moving surfaces ^[20-22]; though, only moderate insights can be obtained about circular jet impingements from their works.

In the area of analytics, the flow of a thin film of water onto a stationary surface is studied using boundary layer theory by Watson ^[15] and results in expressions for velocity fields in four regions: the stagnation region, the boundary layer region, the decreasing free surface velocity region and the hydraulic jump region. Additionally, a mathematical model proposed by Hlod et al. ^[18] describes the interaction of a slow, highly viscous Newtonian jet interact with a slow moving surface. His model is restricted to solely describing the case of deposition (100% transfer efficiency).

In the area of computation, no successful study on circular jet impingement has been carried out with moving surfaces. Olson et al. ^[19] use large eddy simulation to simulate circular jet impingement on a stationary surface. Turbulence statistics and mean velocities along with their streamlines are obtained.

In the area of experimentation, Azuma and Hoshino^[16] experimentally verify Watson's expressions for the boundary layer region and film thickness. However, Stevens and Webb^[17], using laser-Doppler velocimetry across the fluid layer depth show that a maximum velocity in the layer is not at the free surface for $r/d < 2.5$.

In the works of Green et al.^[23 24 25], circular jets impinging on high speed moving surfaces are studied. They conclude that viscous effects play an important role, more so than surface tension, in the determination of deposition/splash boundaries. The surface speeds used in their experiments; however, did not exceed 10m/s. Thus, future work to study the effects of much higher surface speed must be performed to ensure a complete understanding.

1.4. Research Objectives

Little is known about the dynamics of jet impingement on high speed moving surfaces and due to its wealth of applications merits further investigation. In any application of spray coating, the primary objective is to achieve the best possible transfer efficiency, with transfer efficiency defined as the ratio of the amount adhered to the track to the amount sprayed. Methods involving atomized sprays show transfer efficiencies as low as 65% and become even less suitable for higher speed applications. Meanwhile jet impingement can guarantee 100% transfer efficiency under specific conditions.

The main research objective of this project is to continue the study of Green et al.^[23, 24, 25] and extend their findings of Newtonian liquid jet interactions with surfaces to surface speeds in the range of 10m/s to 96m/s.

To achieve such speeds, a rotating 25" diameter disk is used in place of a linear traverse. Centrifugal forces are present; though, resulting accelerations are negligible in comparison to the decelerations involved with any jet impingement. Many spray coating applications involve a stationary surface and a moving nozzle. This condition is not reproduced within laboratory conditions; though, an accurate indication of the dynamics in these cases can, nonetheless, be inferred.

In analyzing the knowledge gained from this investigation, it is hoped that optimal application methods of sprays are defined to achieve maximum transfer efficiencies and to minimize product wastage.

2 Mass Flow Rates

Integral to determining the jet velocity from an applied nozzle back-pressure are flow rate measurements. Pressure is applied to the liquid via a bladder accumulator pressurized by compressed nitrogen. An automated system, discussed further in Appendix A, allows the pressure to be adjusted to within ± 0.1 PSI while a pressure transducer installed close to the nozzle records the pressure.

To measure the mass flow rate, flow is permitted to the nozzle through the activation of a solenoid valve for duration of 2 seconds. This flow is deflected by a flow-interrupter during that period of time to remove potential measurement errors resulting from transient effects due to the initiation of the flow. Following this, the flow-interrupter is de-activated and liquid then flows freely un-interrupted into a cup for collection. The flow is permitted for a total of 15 seconds; meanwhile, the pressure at the 7.5 second mark, is recorded. Finally, the solenoid valve closes and the flow-interrupter is activated to deflect the decaying flow from the collection container. Since the jet diameter and fluid density is known, the jet velocity can be calculated as a function of the applied nozzle back-pressure. Figure 2.1 reports the jet velocity for several nozzle sizes and fluid combinations. The test fluid properties are presented in Table 2.1. Power law fits for the data are presented in Table 2.2 and are in good agreement with an ideal model for the jet velocity as a function of pressure, exhibiting a near square root dependence on pressure. This model, given by Equation 2.3, assumes incompressible flow as well as absence of viscous losses and shows no dependence on the orifice diameter. Given that the pressures used are small enough to prevent significant volumetric compression of the fluids and that the length of the orifices used is $100\mu\text{m}$, the viscous losses are almost negligible, explaining the compliance of the collected data to the idealized model. Technical details of the nozzle assembly are given in Appendix A.

$$V_{Jet} = \frac{4\dot{m}}{\pi\rho d^2} \quad \text{Equation 2.1}$$

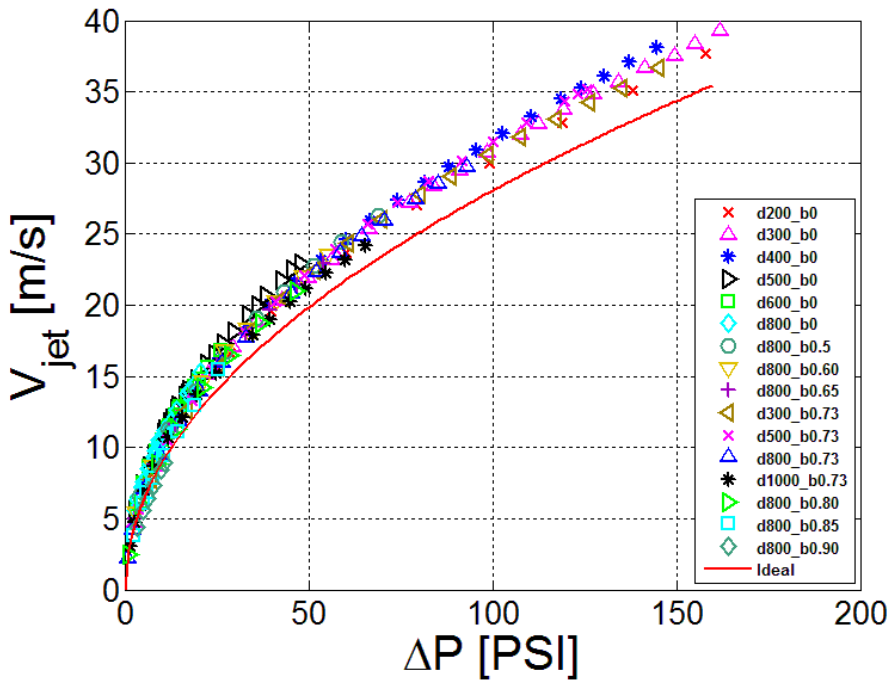
$$\frac{d}{d_o} \cong 0.869^{[23]} \quad \text{Equation 2.2}$$

$$V_{jet_{ideal}} = \left(\frac{d_o}{d}\right)^2 \cdot \sqrt{\frac{2\Delta P}{\rho}} \quad \text{Equation 2.3}$$

Table 2.1 The Composition and properties of Newtonian test liquids at 25 C

Fluid	ρ [kg.m]	μ [mPa.s]
0% glycerin + water	997.08	0.9
50% glycerin + water	1123.75	5.1
60% glycerin + water	1151.05	9.0
65% glycerin + water	1164.75	12.5
73% glycerin + water	1186.50	24.3
80% glycerin + water	1205.45	47
85% glycerin + water	1218.70	83.5
90% glycerin + water	1232.00	164

Figure 2.1 Calculated Jet Speed from MFR



$$V_{Jet} = a \cdot (\Delta P)^b \quad \text{Equation 2.4}$$

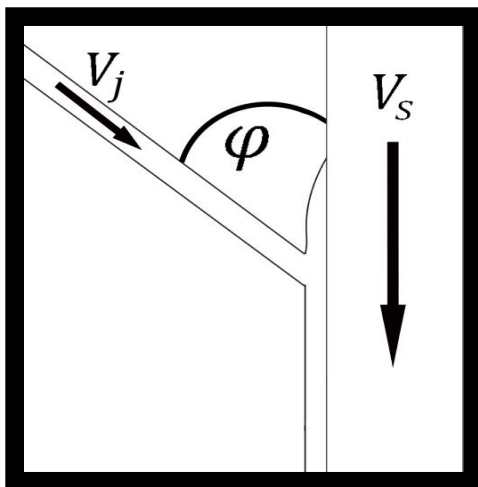
Table 2.2 Empirical Fit Parameters

NOZZLE, FLUID COMBINATION	a	b	r^2
200µm, 0% glycerin + water	3.3091	0.4804	0.9996
300µm, 0% glycerin + water	3.1241	0.4985	0.9991
400µm, 0% glycerin + water	3.3173	0.4899	1.0
500µm, 0% glycerin + water	3.4105	0.4943	0.9997
600µm, 0% glycerin + water	3.3458	0.4953	0.9998
800µm, 0% glycerin + water	3.3046	0.5056	0.9982
800µm, 50% glycerin + water	3.2547	0.494	0.9994
800µm, 60% glycerin + water	3.0147	0.5146	0.9993
800µm, 65% glycerin + water	2.9772	0.5145	0.9996
300µm, 73% glycerin + water	2.9424	0.5102	0.9983
500µm, 73% glycerin + water	2.958	0.5147	0.9994
800µm, 73% glycerin + water	2.6687	0.5391	0.9968
1000µm, 73% glycerin + water	2.7941	0.5235	0.9967
800µm, 80% glycerin + water	2.576	0.5537	0.9985
800µm, 85% glycerin + water	2.3643	0.5822	0.9975
800µm, 90% glycerin + water	2.1268	0.5987	0.9999

3 Water Tests

The interaction of a jet of water with a high-speed moving surface was captured using high-speed photography. The jet diameter, impingement angle, jet speed and surface speed were independently varied. In these tests orifices 200 μm , 300 μm , 400 μm , 500 μm , 600 μm , and 800 μm in diameter produced jets that impinged on a surface at one of 5 angles, namely, 35 $^\circ$, 60 $^\circ$, 90 $^\circ$, 135 $^\circ$, and 160 $^\circ$ measured from the negative V_s vector. Jet and surface speeds were both varied within a range of 5-50m/s. Figure 3.1 shows a schematic of a jet moving at V_j impinging on a surface moving at, V_s at an angle of φ .

Figure 3.1 Schematic of Impingement



Three distinct categories describe the outcomes of these tests, namely, deposition Figure 3.2a, spatter Figure 3.2b and lift-off Figure 3.2c. In the case of deposition no fluids leave the surface while in the alternative cases of spatter or liftoff fluids leave the surface. When spattering occurs, ripples at the leading edge of the lamella that would otherwise remain part of the lamella leading edge in the case of deposition detach and leave the surface. When lift-off occurs, a sheet of fluid undergoes sustained lift and entirely leaves the surface.

Figure 3.2 Three Categories of Impingement

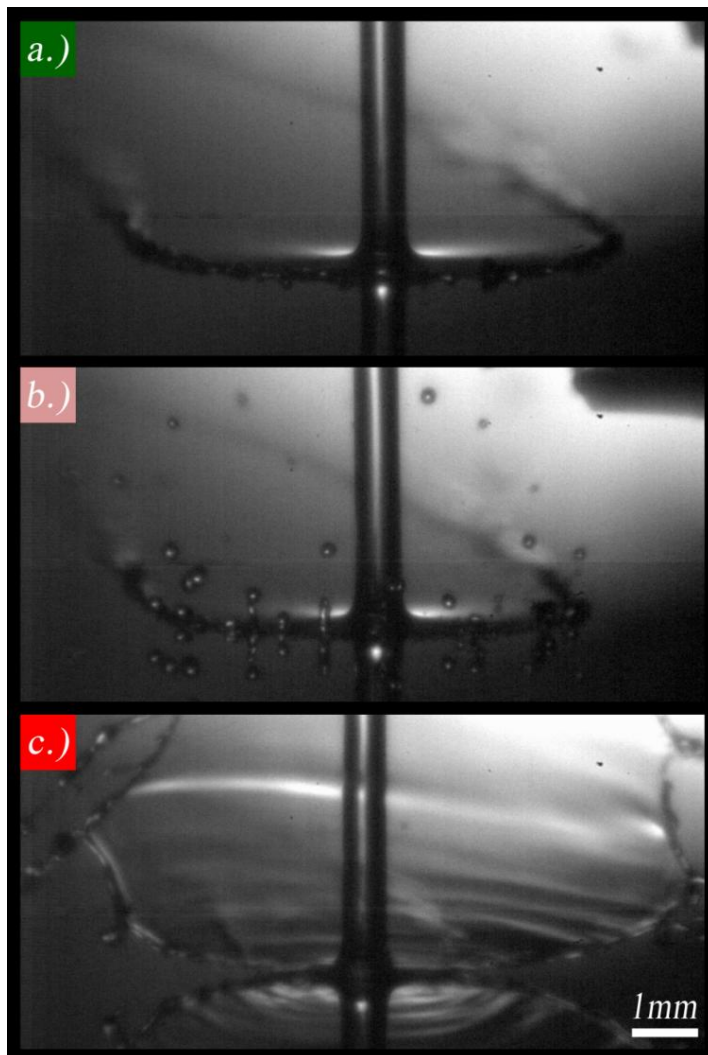
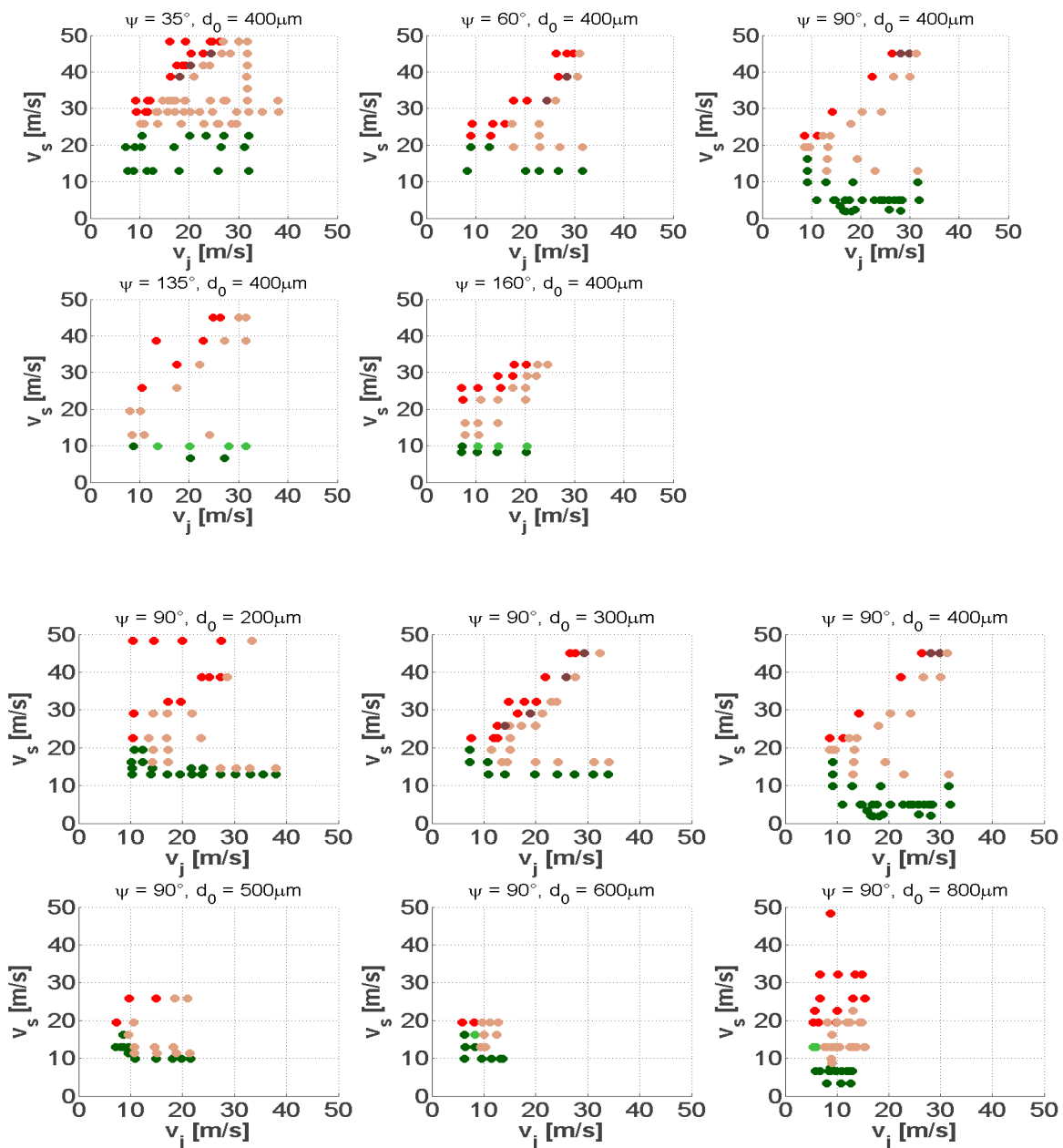


Figure 3.3 plots the results for experiments performed at variable impingement angles, φ , for a constant orifice diameter, $d_0 = 400\mu m$ as well as results of experiments performed at a constant impingement angle, $\varphi = 90^\circ$, for variable orifice diameters, d_0 . These figures plot jet speed versus surface speed, encoding the result of the experiment by color. A total of five colors are used, three to identify the categories described previously and two more to identify transition points between these two categories whereby the experimental result appears to be in a superposition of two of the three categories, indicative of either weak deposition or weak lift-off. Table 3.1 identifies the colors used and their associated meanings.

Table 3.1 Water Test Legend

Color	Name	Description
Dark Green	Deposition	No fluids leave the surface.
Light Green	Weak Deposition	A small number of droplets occasionally leave the surface.
Light Brown	Spatter	Droplets frequently leave the surface.
Dark Brown	Weak Lift Off	Droplets frequently leave the surface. A sheet occasionally appears.
Red	Lift Off	A sheet forms and lifts off of the surface.

Figure 3.3 Results of Water Impingement



In Figure 3.3 one easily observes a threshold at which deposition transitions to spatter and another where spatter transitions to lift-off. The first threshold, named the lower threshold, consistently follows the pattern of a straight, horizontal line beyond 10m/s surface speed throughout all the tests while the second threshold, named the upper threshold, follows a diagonal line along the V_j, V_s plot. Figure 3.4 shows the dependence of these thresholds as a function of the angle, φ , for a fixed $d_0 = 400\mu m$ and as a function of d_0 for a fixed $\varphi = 90^\circ$.

Figure 3.4 Extracted Boundary Information

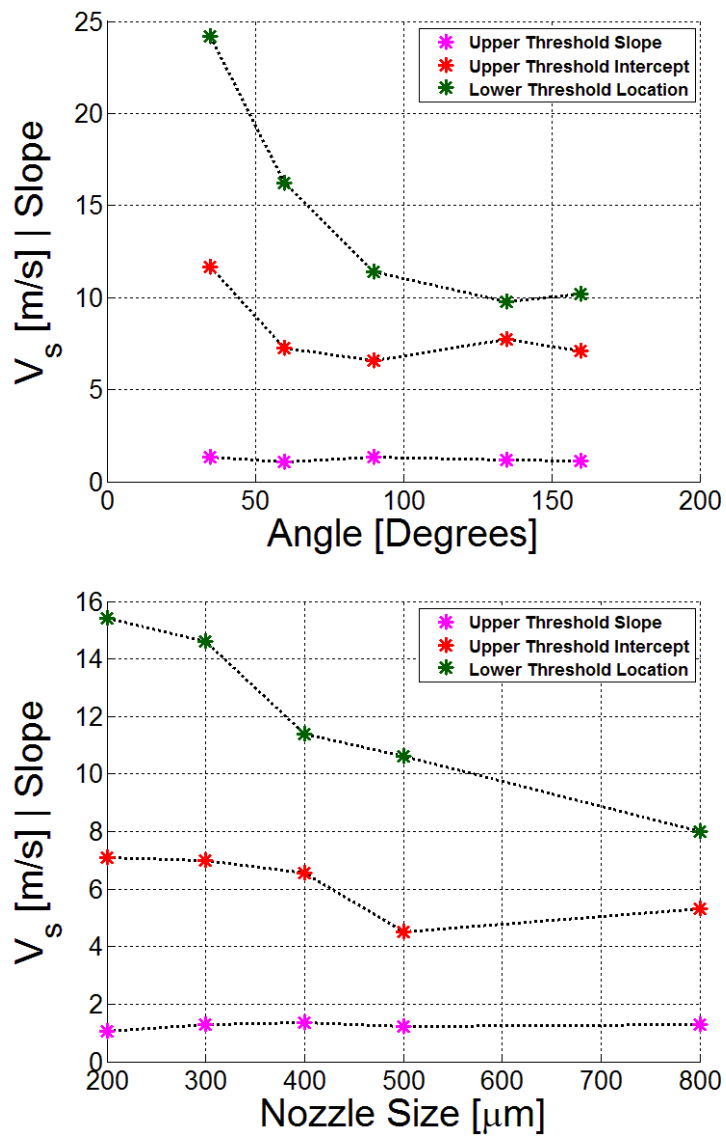


Figure 3.4 shows that the slope of the upper threshold is invariant to the angle or nozzle size; though, the V_s intercept of the upper threshold line appears to decrease slightly, indicating that the location of the threshold decreases as angle or nozzle diameter increases. The lower threshold location decreases more significantly as angle or nozzle diameter increases. Being that the lower threshold indicates the lowest value for V_s where fluids first begin to leave the surface, one can conclude that fluids will more readily leave the surface for larger angles measured from the negative V_s vector.

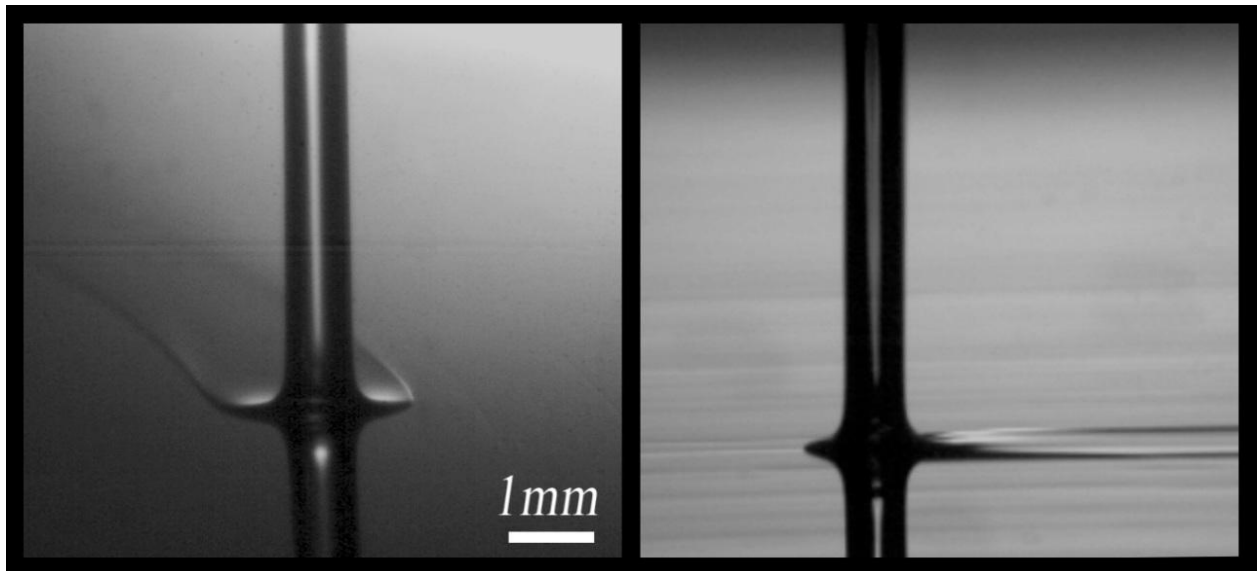
It is postulated that jets with larger components of velocity parallel to the surface velocity relative to their perpendicular components are more likely to deposit. Larger jet diameters are expected to produce larger spread radii, R , the amount the lamella spreads ahead of the jet in the upstream direction, which is thought to enhance the probability of lamella lift-off due to an increased susceptibility to acquire sustained aerodynamic lift upon any momentary detachment from the surface.

Many experiments were performed with jets of water to demonstrate the effects of angle, nozzle size, surface velocity and jet velocity. Three distinct categories describe the outcomes of these tests, namely, deposition Figure 3.2a, spatter Figure 3.2b and lift-off Figure 3.2c. Transitions from deposition to spattering show a definitive dependence on the surface velocity. It was observed that decreased angles measured from the negative surface velocity vector promoted deposition for all nozzle sizes explored while decreased nozzle sizes promoted deposition for all angles explored. It is postulated that the ratio of $V_{||}$ to the magnitude of \vec{V}_s is a significant quantity in predicting the likelihood of deposition occurring for acute angles.

4 Water-Glycerin Tests

A series of experiments were conducted with water-glycerin solutions of 60% weight glycerin or greater using 300 μm , 500 μm , 800 μm , and 1000 μm orifice diameters with impingement angles of 35 $^\circ$, 60 $^\circ$, 90 $^\circ$ and 135 $^\circ$ to study the interaction of higher viscosity jets with a polished moving surface. Surface speeds were varied between 8m/s to 96m/s while jet speeds were varied between 7m/s to 37m/s. The results showed that deposition occurred for almost every configuration on clean surfaces whenever a stable jet was achieved. Figure 4.1 shows two camera angles of a 695 μm jet (from an 800 μm orifice) impinging on a surface moving 100m/s.

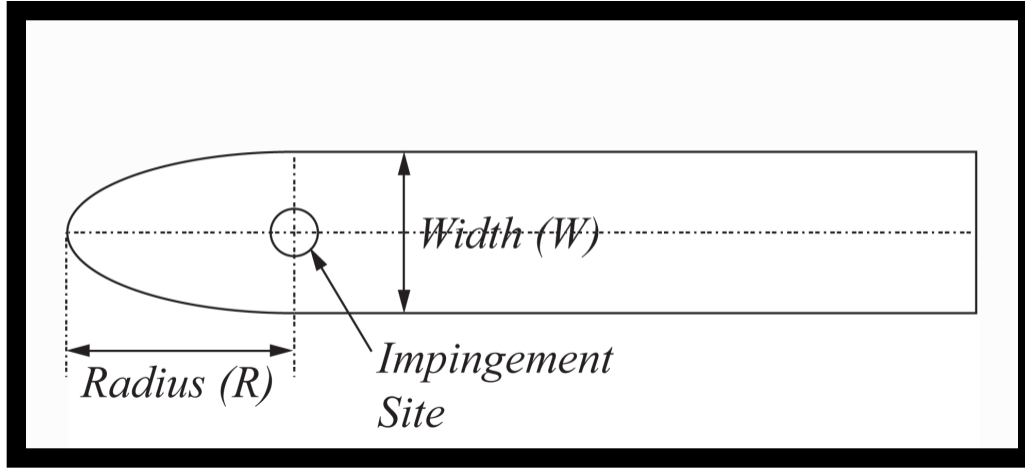
Figure 4.1 Deposition of 73%g.w. for $V_s = 96\text{m/s}$, $V_j = 15\text{m/s}$ $\varphi = 90^\circ$, $d = 800\mu\text{m}$



4.1. Lamella Dimensions

Follow from the work of Kumar et al. ^[24], a more extensive analysis of spread width and spread radius for a glycerin-water solution was performed. Spread radius, R , is defined as the maximum distance the lamella spreads ahead of the impingement site while spread width, W , is defined as the sum of the distances on either side of the impingement site. Figure 4.2 identifies these definitions.

Figure 4.2 Spread Width and Spread Length Schematic



The shape and dimensions of the lamella depend on the inertial (φ, d, V_j, V_s) and fluid parameter of the jet (ν). Two camera angles facilitated the measurement of both W and R . Distance S_p was measured in units of pixels as viewed on a computer monitor. R_p and W_p measurements (measured in units of pixels) were then compared to the jet diameter D_p (measured in units of pixels). The image fuzziness δS_p (measured in units of pixels) was also taken and recorded for the sake of error analysis. Equation 4.1 describes how S is calculated from pixel measurements of a pattern within the image and the jet diameter while Equation 4.2 describes the error in the value S . Equation 4.3 defines the Reynolds number with the surface speed and the jet diameter.

$$S = \frac{S_p}{d_p} \quad \text{Equation 4.1}$$

$$\delta S = \pm \delta S_p \cdot \sqrt{\frac{1+S_p}{d_p^2}} \quad \text{Equation 4.2}$$

$$Re = \frac{V_s \cdot d_o}{\nu} \quad \text{Equation 4.3}$$

Figures 4.4 and 4.5 plot the experimental results with error bars and weighted fits for varied conditions, namely, surface speeds, V_s , jet diameters, d , and impingement angles, φ . In Figure 4.5 only data for inclination angle of 90° were used to determine the line of best fit. Figure 4.4 plots R versus W for varied impingement angles, φ . In Figures 4.4 and 4.5 it can be seen that the spread radius and spread width

measured in jet diameters increases for increased jet speed to surface speed ratios, increased jet diameters, decreased kinematic viscosity and increased impingement angles. Evidently, $\frac{W}{d}$ does not scale with angle the same way that $\frac{R}{d}$ does; though, $\frac{W}{d}$ scales similarly for other variables.

Figure 4.3 Radius vs Width of 73%g.w. for $V_s = 32\text{m/s}$, $V_j = \text{varied}$ $\varphi = \text{varied}$, $d = 800\mu\text{m}$

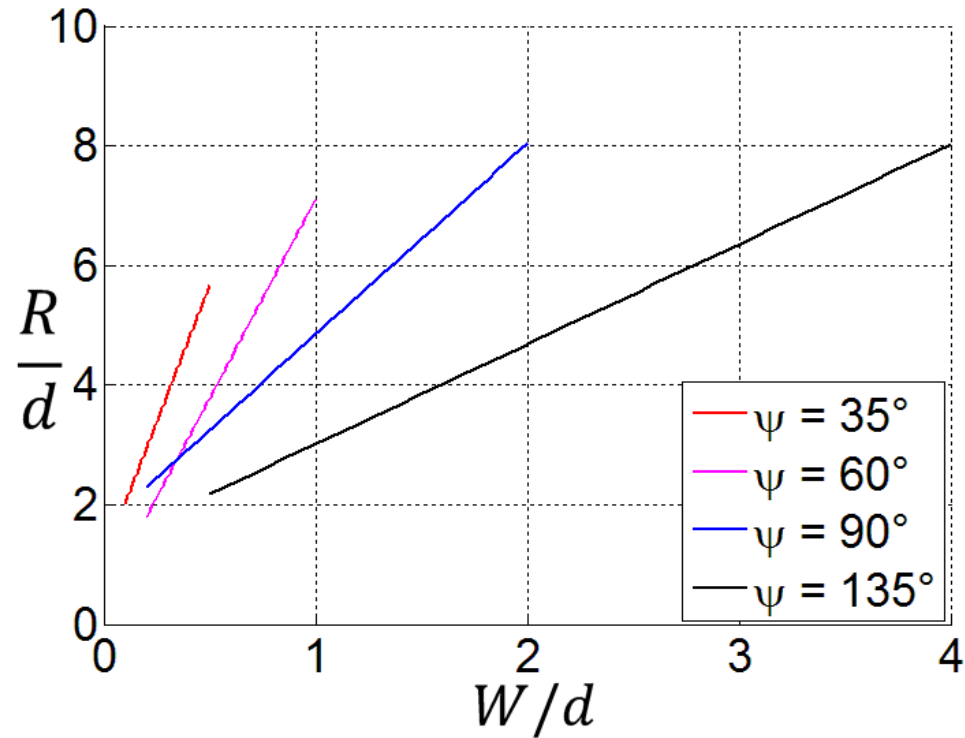


Figure 4.4 Non-dimensional data (Radius)

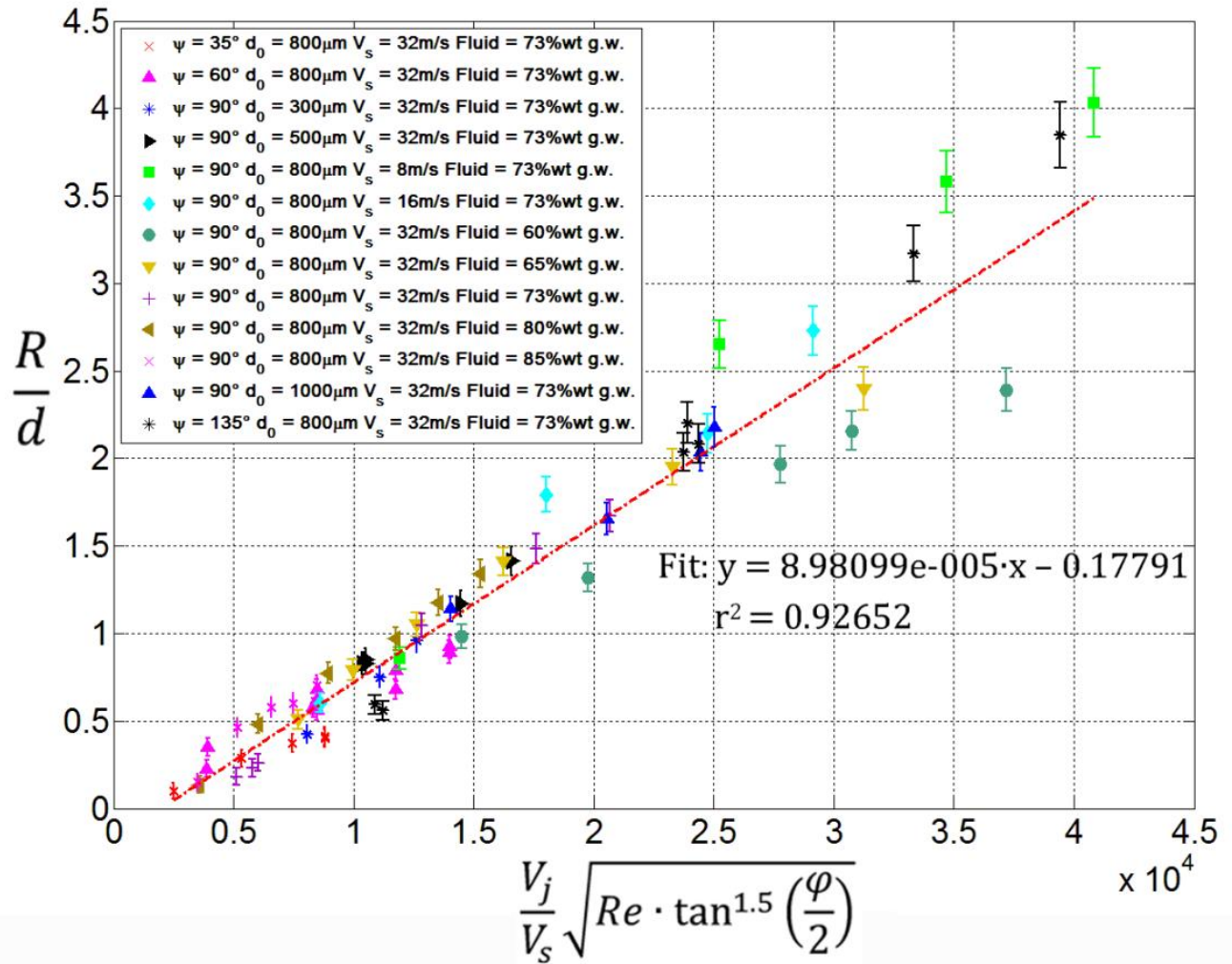
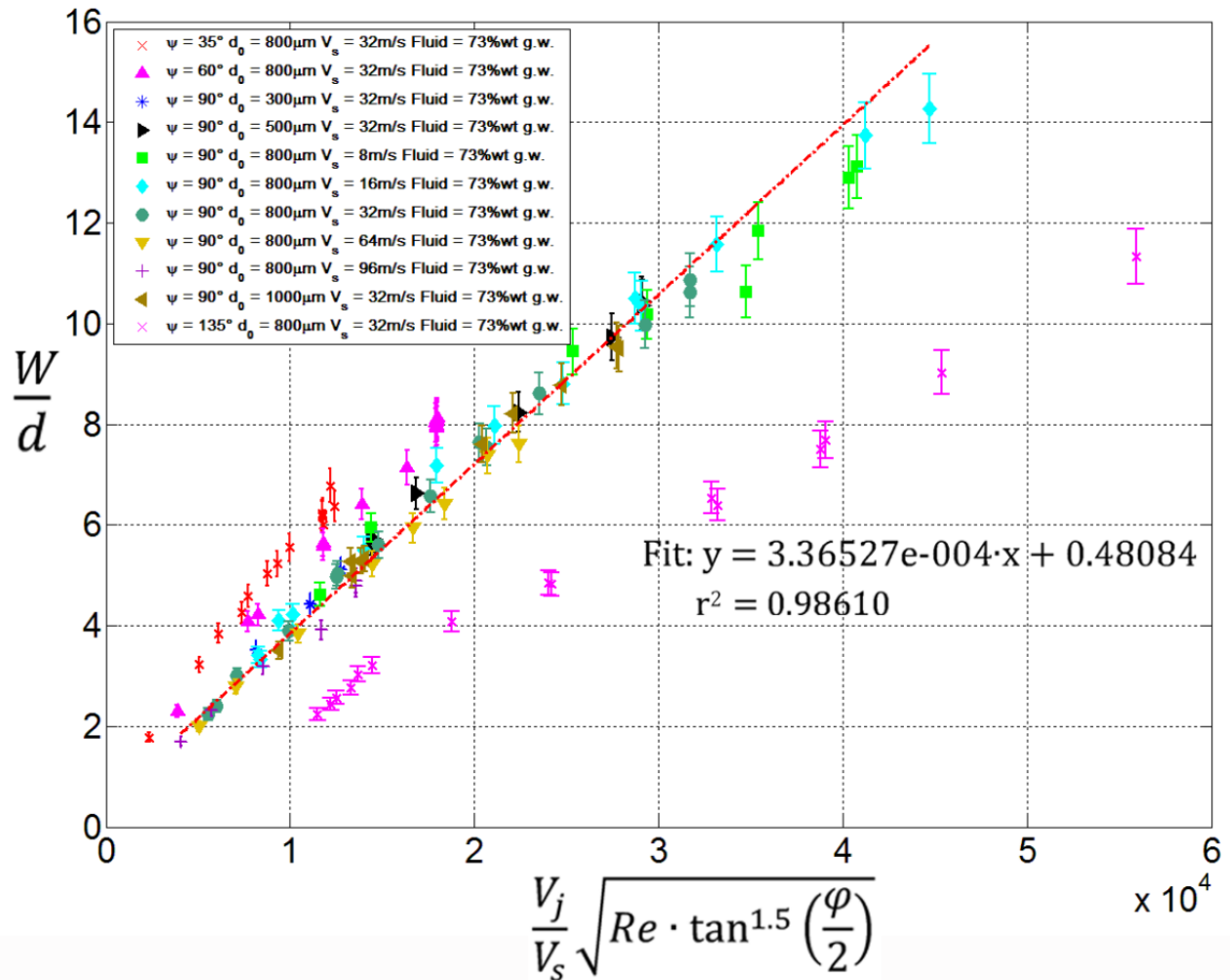


Figure 4.5 Non-dimensional data (Width)



Many experiments confirm viscous jets moving in the range of 7m/s to 37m/s will impinge on a smooth surface moving at speeds in the range of 8m/s to 96m/s. Measurements of the spread radius and spread width were taken for varied V_j , V_s , d , ν , and ϕ . The spread radius and width are both observed to increase with increased jet speed to surface speed ratios, increased jet diameters, decreased kinematic viscosity and increased impingement angles.

5 Triggering and Recovery

It has been observed that, for a variety of surface and jet conditions, jets will deposit cleanly on surfaces (Figure 5.2c). In addition it has been observed that these liquids that deposit can be transitioned to a state of self-sustained lamella lift-off (Figure 5.2d). It has been observed that several different mechanisms can trigger the transition to lamella lift-off: jet instabilities (Figure 5.1b), interaction with liquid droplets adhered to the surface (Figure 5.1e), and surface discontinuities near the impingement location (Figure 5.1h).

Figure 5.1 Oncoming view of impingement of a jet from an 800 μm orifice oriented at $\varphi = 60^\circ$ with surface motion into the page. $V_j = 17\text{m/s}$, $V_s = 16\text{m/s}$. (Left to Right) (a) Deposition prior to jet instability interaction (b) Jet instability interaction (c) Self-sustained lift-off (d) Deposition prior to interaction with droplets on surface (e) Interaction with droplets on surface (f) Self-sustained lift-off (g) Deposition prior to interaction with 250 μm step discontinuity, (h) Interaction with 250 μm step discontinuity, (i) Self-sustained lift-off.

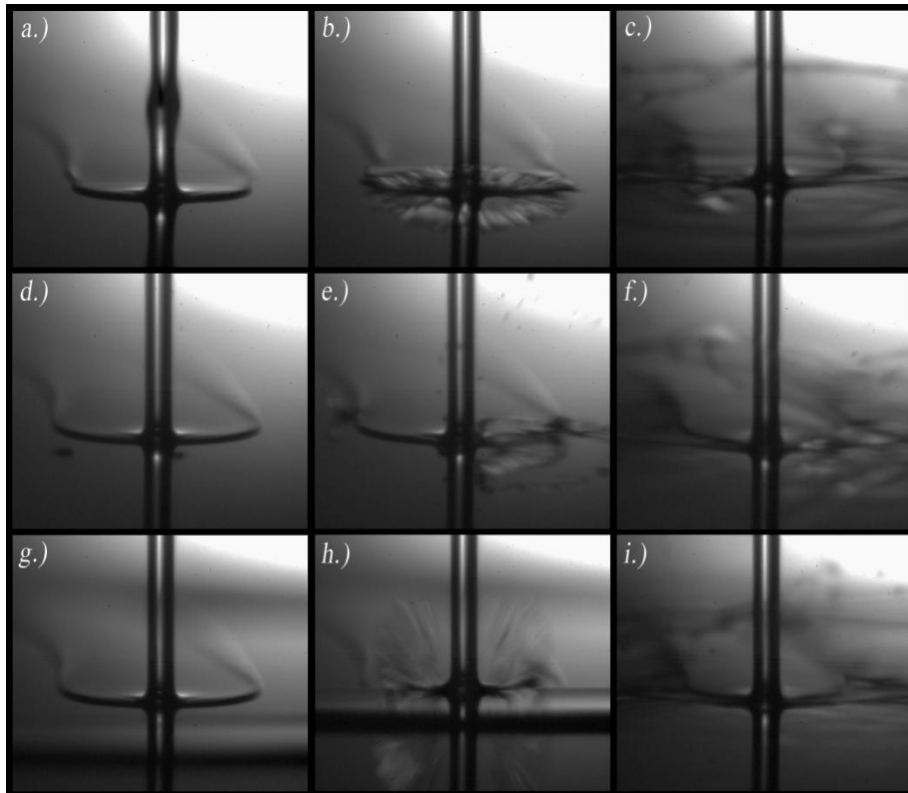
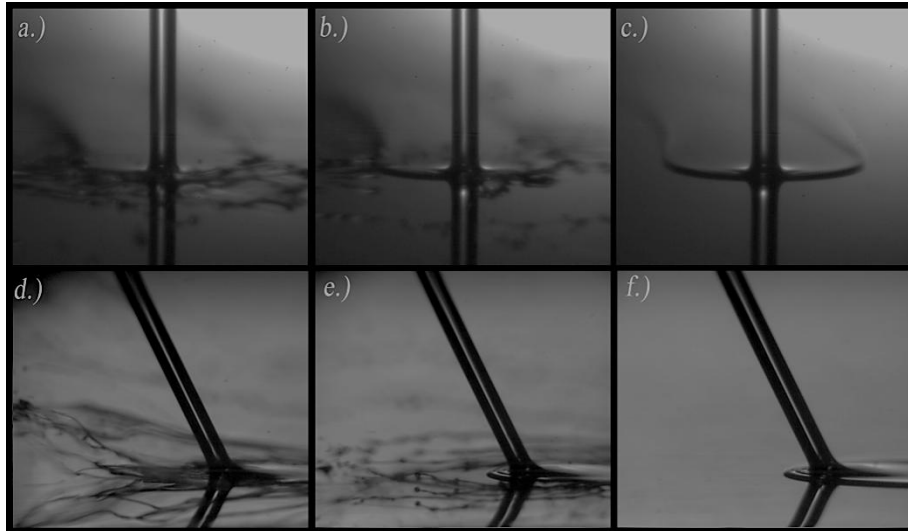
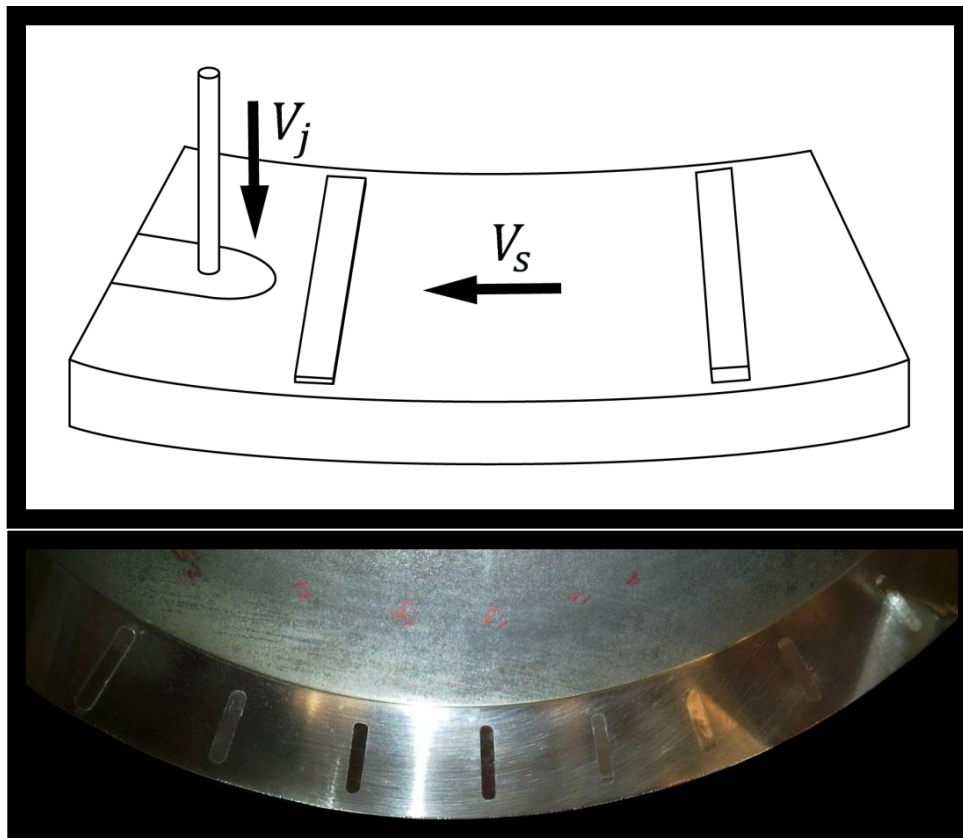


Figure 5.2 Top view and side view of recovery of a jet from an 800 μm orifice oriented at $\varphi = 60^\circ$. $V_j = 17\text{m/s}$, $V_s = 16\text{m/s}$. (Left to Right) (a, d) Breakup of lamella sheet, (b, e) Partial recovery, (c, f) Full recovery.



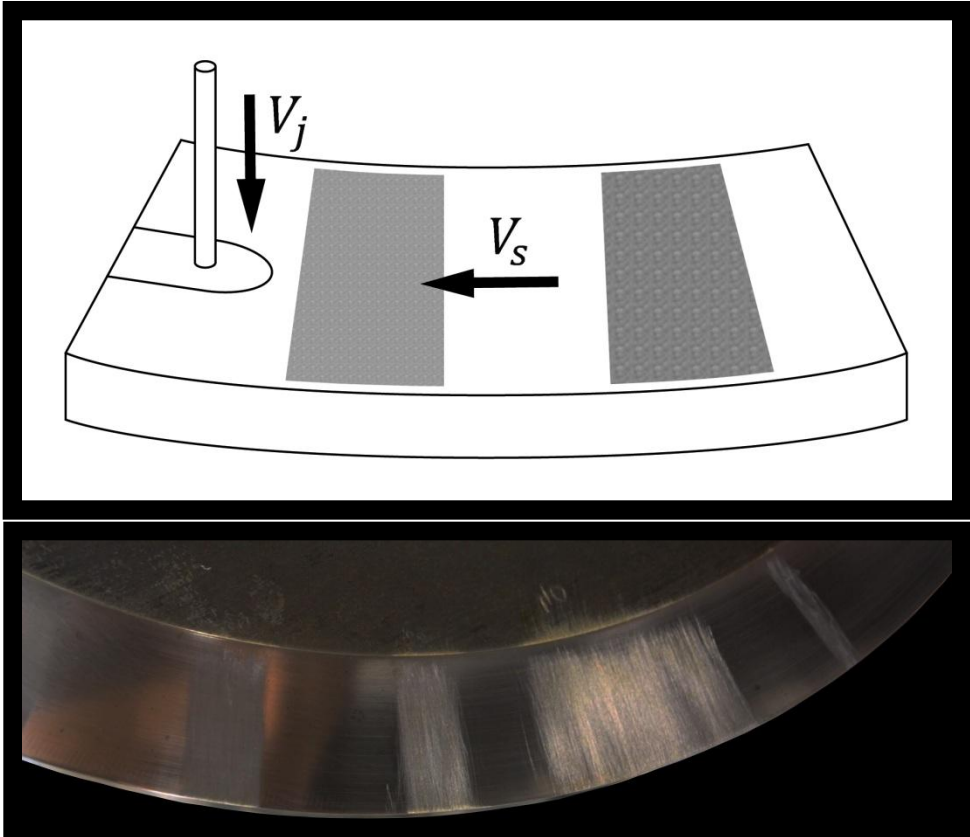
To determine the size of the smallest surface discontinuity that could trigger transition to lift-off, a series of increasing step heights (Figure 5.3) were formed by adhering rectangular strips to the surface. Step heights as small as 30 microns were found to consistently trigger a transition from deposition to lift-off. Lift-off can occur over track distances of several thousand jet diameters. Upon attaining a state of self-sustained lamella lift-off, it is then possible to return to a state of deposition, which is referred to as “recovery”. The distance between the lamella lift-off point and the return to deposition is referred to as the “recovery length”. The process of recovery appears to be stochastic, with an occurrence probability influenced by the presence of jet instabilities, surface discontinuities, previously adhered liquid droplets, and surface roughness. These triggers lead to random hydrodynamic fluctuations, causing a sheet of liquid in sustained lift-off, named the lift-off sheet, to breakup. This permits 100% deposition of the liquid from the jet. Under certain conditions recovery appears to occur spontaneously. It is hypothesized that in these cases unobservable random hydrodynamic fluctuations from the incoming jet and/or random aerodynamic fluctuations in the surrounding air are responsible for the breakup of the lift-off sheet.

Figure 5.3 Intentional Surface Discontinuity



To determine the effects of surface roughness on recovery, several patches of track were roughened to varied degrees (Figure 5.4) and the length of track covered until recovery of a jet previously triggered to a state of sustained lamella lift-off was monitored. For all cases there was a dramatic reduction in the average distance covered until recovery occurred. Test conditions that on a well-polished surface would have a long recovery length had a recovery length up to two orders of magnitude shorter on a roughened surface.

Figure 5.4 Intentional Surface Roughness



6 Repeatability Tests

To study the phenomena of recovery, experimental variables were selected that could be repeatedly triggered to splash and that would recover within the polished track length. A surface discontinuity created by a 250 μ m rectangular strip of stainless sheet steel adhered to the surface was used as a trigger. Jet impingement upstream of the surface discontinuity was characterized by complete deposition. Immediately following the trigger self-sustaining lamella lift-off would be observed for the recovery length, after which a transition from lamella lift-off to deposition would be observed.

It is postulated that random fluctuations of the incoming jet and/or surrounding air give rise to the possibility of recovery. These fluctuations are frequent and invariant to the track location. Thus, the probability of any one of these two types of fluctuations occurring maintains a constant value over the track length. Upon any single fluctuation, a very small probability to recover exists. This probability to recover is also independent of the impingement location on the track and also maintains a constant value over the track length. Therefore the probability of recovery occurring due to a single random fluctuation will be small and will maintain a constant value over the track length. Denoting the event of a random fluctuation, E_f , and the event of recovery, E_r , the previous statement is expressed in Equation 6.1.

$$p = P(E_f \cap E_r) = P(E_r|E_f) \cdot P(E_f) \quad p \ll 1 \quad \text{Equation 6.1}$$

The probability of seeing a chance to recover k times after the occurrence of N random fluctuations is then given by the binomial distribution:

$$P(X_N = k) = \binom{N}{k} \cdot p^k \cdot (1 - p)^{N-k} \quad \text{Equation 6.2}$$

Given that p is small and that N is very large, the random variable X_N is well approximated as a poisson random variable. Taking $Np = \lambda \cdot D_s$, the probability to see k recoveries over a distance D_s is given by Equation 6.3

$$P(Y = k) = \frac{(\lambda D_s)^k}{k!} \cdot e^{-\lambda D_s} \quad \text{Equation 6.3}$$

The probability to see no recovery after distance D_s is then given by Equation 6.4

$$P(Y_{D_s} = 0) = e^{-\lambda D_s} \quad \text{Equation 6.4}$$

This is equivalent to saying that the recovery length, L , is greater than D_s

$$\{L > D_s\} = \{Y_{D_s} = 0\} \quad \text{Equation 6.5}$$

Thus by complementarily the probability to see at least one recovery after distance D_s is given by

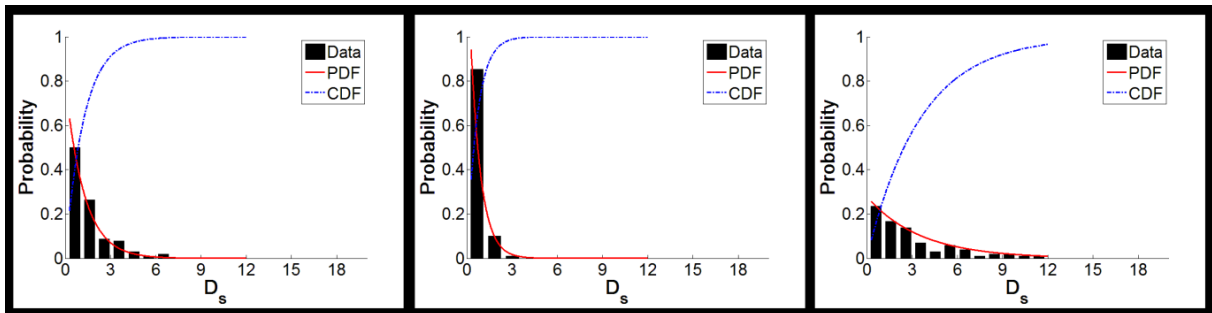
$$Cdf = P(L \leq D_s) = 1 - e^{-\lambda D_s} \quad \text{Equation 6.6}$$

The above equation represents the cumulative probability distribution; differentiation leads to the probability density function given below

$$Pdf = f(D_s) = \lambda \cdot e^{-\lambda D_s} \quad \text{Equation 6.7}$$

This function is used to fit the collected data shown in the histograms below whose horizontal axis shows the recovery distance measured in track partitions and whose vertical axis, representative of the statistical probability of occurrence indicates the frequency normalized by the total number of experiments performed for each case (100). In order to display a normalized Pdf and Cdf , the 1.94m track length is partitioned into a total of 12 sections.

Figure 6.1 Recovery probability v.s. Track partitions (Left to Right)



The resulting fit parameter and respective correlation coefficient value is tabulated in Table 6.1 along with the details of the experimental configuration.

Table 6.1 Experimental configuration values and resulting curve fit data

Parameter Set	Fluid	φ	d	V_j [m/s]	V_s [m/s]	Fitted λ	r^2
P ₁	73% g + 27% w	60 ⁰	695	17	16	0.8018	0.9699
P ₂	73% g + 27% w	90 ⁰	695	20	32	1.4578	0.9441
P ₃	73% g + 27% w	135 ⁰	695	13	16	0.2806	0.9786

In this study viscous jet impingement onto a high-speed moving surface has been investigated. In particular, transition from self-sustained lamella lift-off to deposition has been investigated. Many configurations that exhibit deposition can be triggered to exhibit self-sustaining lamella lift-off. The lamella lift-off is susceptible to disturbances and may transition back to steady deposition. Repeated tests within a constant parameter set have shown that the transition from lift-off to deposition is a stochastic phenomenon that is well modeled by a Poisson process.

7 Conclusions and Recommendations for Future Work

An experimental setup to study jet impingement on surfaces moving at speeds up to 96m/s was designed and built. High speed photography at two different camera angles was employed to capture the interaction of Newtonian liquid jets of varied diameters and impingement angles with the high speed moving surface. Conditions at the surface were varied through additions of surface discontinuities and roughened patches. Spread radii and widths were recorded along with transition track lengths for chosen sets of experiments.

7.1. Conclusions for Water Tests

Many experiments were performed with jets of water to demonstrate the effects of angle, nozzle size, surface velocity and jet velocity. The key findings are:

- Three distinct categories describe the outcomes of these tests, namely, deposition, spatter and lift-off.
- Transitions from deposition to spattering show a definitive dependence on the surface velocity.
- Smaller nozzle sizes promote deposition.
- Smaller impingement angles (measured from the negative surface velocity vector) promote deposition.

7.2. Conclusions for Water-Glycerin Tests

7.2.1 Conclusions for Lamella Dimensions

Many experiments confirm viscous jets moving in the range of 7m/s to 37m/s will impinge on a smooth surface moving at speeds in the range of 8m/s to 96m/s. Measurements of the spread radius and spread width were taken for varied V_j , V_s , d , ν , and φ . The key findings are:

- The spread radius and width are both increase with increased jet speed to surface speed ratios.
- The spread radius and width both increase with increased jet diameters.
- The spread radius and width both increase with decreased kinematic viscosity and increased impingement angles.
- The spread width scales similar to the spread radii for all variables except φ .

7.2.2 Conclusions for Triggering and Recovery

Transitions from self-sustained lamella lift-off to deposition has been investigated. Viscous jets were made to deposit onto a moving surface. Deposition is then intentionally triggered to self-sustained lamella-liftoff and the track length covered until recovery back to the original state of deposition was recorded for several configurations. The key findings are:

- Surface roughness can have dramatic effects on the recovery length.
- Recovery is a stochastic phenomenon well modeled as a Poisson process.
- Deposition can be triggered to lamella-liftoff and vice versa via triggers such as: jet instabilities, interaction with liquid droplets adhered to the surface, and surface discontinuities near the impingement location.

7.3. Recommendations for Future Work

Studies of Newtonian liquid jet impaction on a high speed moving surface provide design implications for an industrial sprayer. The accomplished experiments indicate that deposition onto surfaces moving up to 96m/s is possible for Newtonian liquids of sufficiently high viscosity and that shallow angles as measured from the negative surface velocity vector will enhance transfer efficiencies. Results also tend to recommend the use of duty cycling due to the potential for states of deposition to transition to undesirable states of self-sustained lamella lift-off.

There is still much work which has the potential to continue to offer valuable practical advice. Some interesting developments which should continue with this project include:

- An analysis of the effects of crosswinds on deposition and recovery.
- An analysis of the difference between moving the surface rather than the nozzle.
- An analysis of the effects of non-Newtonian fluids.
- An analysis of the correlation between transfer efficiencies and lamella dimensions.
- An analysis of the effect of duty cycling on deposition and recovery.

Bibliography

- [1] Eadie, D.T., Bovey, E., and Kalousek, J. (2002), The role of friction control in effective management of the wheel/rail interface, Railway Technical Conference, November 2002.
- [2] Eadie, D.T., and Kalousek, J. (2001), Spray it on, Let'em Roll, Railway Age.
- [3] Cotter, J., Eadie, D.T., Elvidge, D., Hooper, N., Robert, J., Makowsky, T., and Liu, Y., 2005. Top of Rail Friction Control: Reductions in Fuel and Greenhouse Gas Emissions. In: Proc. Of the 2005 Conference of the International Heavy Haul Association (Rio de Janeiro), pp. 327-334.
- [4] Li, L.K.B., Dressler, D.M., Green, S.I., Davy, M.H., and Eadie, D.T., 2009. Experiments on Air-Blast Atomization of Viscoelastic Liquids, Part 1: quiescent Conditions. *Journal of Atomization and Sprays*, 19:157-190.
- [5] Li, L.K.B., Green, S.I., Davy, M.H., and Eadie, D.T., 2010, Air-blast atomization of viscoelastic liquids in a cross-flow, Part 1: Spray Penetration and Dispersion, accepted for publication in *Journal of Atomization and Sprays*.
- [6] Courbin, L., Bird, J.C., and Stone, H.A., 2006, Splash and anti-Splash: Observation and Design., *Chaos*, 16:041102.
- [7] Gregory, P. H., et al., *J. Gen. Microbiol.* 20, 328 (1959).
- [8] Liu, Q., Orme M., (2001), High precision solder droplet printing technology and the state-of-the-art. *Journal of Materials Processing Technology*, 115:271-283
- [9] Rioboo, R., Marengo, and M., Tropea, C, 2002, Time Evolution of Liquid Drop Impact onto Solid, Dry Surfaces, *Experiments in Fluids*, 33:112-124.
- [10] Okawa, T., Shiraishi, T., and Mori, T., 2008, Effect of impingement angle on the outcome of single drop impact onto a plane water surface, *Experiments in Fluids*, 44:331-339.
- [11] Povarov, O.A., Nazarov, O.I., Ignat'evskaya, L.A., and Nikol'Skii, A.I., 1976, Interaction of drops with boundary layer on rotating surface, *Journal of Engineering Physics*, 31:1453-1456.
- [12] Fathi, S., Dickens, P., and Fouchal, F., 2010, Regimes of droplet train impact on a moving surface in an additive manufacturing process, *Journal of Material Processing Technology*, 210:550-559.
- [13] Fujimoto, H., Suzuki, Y., Hama, T., Takuda, H., 2011, Flow characteristics of circular liquid jet impinging on a moving surface covered with a water film, *ISIJ International*, Vol. 51 (2011), No. 9, pp. 1497-1505
- [14] Bird, J. C., Tsai, S.S.H., and Stone, H.A., 2009, Inclined to Splash: Triggering and Inhibiting a Splash with Tangential Velocity, *New Journal of Physics*, 11 :1 -6(2009).

- [15] E.J. Watson (1964), The radial spread of a liquid jet over a horizontal plane, *J. Fluid Mech.*, 20, 481–495.
- [16] T. Azuma, T. Hoshino (1984), The radial flow of thin liquid film, *Trans. Jpn. Mech. Engrs.*, 50, 974–1136.
- [17] J. Stevens, B.W. Webb (1993), Measurements of flow structure in the radial layer of impinging free-surface liquid jets, *Int. J. Heat Mass Transfer*, 36 (15), 3751–3758.
- [18] Hlod, A., AArts, A.C.T., van de Ven, A.A.F., and Peletier, M.A., 2007, Mathematical model of falling of a viscous jet onto a moving surface, *European Journal of Applied Mathematics*, 18:659-677.
- [19] Olson, M., Fuchs, L., 1998, Large eddy simulations of a forced semiconfined circular impinging jet, *Physics of Fluids Vol. 10, Number 2*.
- [20] Zumbrunnen, D.A. 1991, Convective heat and mass transfer in the stagnation region of a laminar planar jet impinging on a moving surface, *Journal of Heat Transfer*, 113:3 563-570.
- [21] Chattopadhyay, H., Saha, S.K., 2002, Simulation of laminar slot jets impinging on a moving surface, *Journal of Heat Transfer*, December 2002, Vol. 124.
- [22] Senter, J., Sollicec, C., Flow field analysis of a turbulent slot air jet impinging on a moving flat surface, *Journal of Heat and Fluid Flow* August 2006, 708-719.
- [23] Keshavarz, B., 2011, Newtonian and elastic liquid jet interaction with a moving surface, M.A.Sc. Thesis, UBC.
- [24] Kumar, P., 2011, Liquid jet interaction with a moving surface, M.A.Sc. Thesis, UBC.
- [25] Keshavarz, B., Green, S. I., Davy, M. H., and Eadie, D. T., 2010, Newtonian liquid jet impaction on a high speed moving surface, submitted to *International Journal of Heat and Fluid Flow*.
- [26] Gradeck, M., Kouachi, A., Dani, A. Arnoult, D., Boréan, J.L., 2006, Experimental and numerical study of the hydraulic jump of an impinging jet on a moving surface, *Experimental Thermal and Fluid Science* 30 (2006) 193-201

Appendices

Appendix A: Equipment and Usage

This chapter describes the experimental setup used in the present investigation. An overview of the experimental setup will be given, including procedure specifics, then the motor, axle and disk, used as a means to provide a very high speed moving surface, will be addressed. The safety enclosure, nozzle assembly, imaging devices and auto-pressure control unit, hereinafter denoted as the APC, will then be discussed. Finally, a detailed description of the automation setup used, specifically the control box and software, will be put forth.

A.1. Device Summary

To study the role of surface speed on jet impingement, an apparatus capable of producing surface speeds at the impingement location of up to 360 km/h was built. Schematically shown in Figure A.1, the impingement location is at a radius of 30cm on a well-balanced 63 cm diameter polished steel disk. Two high intensity light sources illuminate the impingement location and a high speed Phantom V611 camera records images at 10,000 frames per second from either of two camera angles. A controllable jet speed between 5 m/s and 45 m/s is generated by a bladder accumulator pressurized by compressed nitrogen. A solenoid-actuated flow interrupter removes most transient effects associated with the startup of the jet. In addition to jet and surface speed, variables that have been studied include jet diameter (between 174 microns and 869 microns), impingement angle (35° to 135°), and liquid properties. Almost all tasks involved in reaching a test condition have been automated to ensure consistency in the experimental results.

To conduct a test, the steel disk is first cleaned and dried thoroughly. The accumulator is filled with the test fluid and pressurized with nitrogen to a pressure between 70 and 1100 kPa (corresponding with jet velocities between 5 and 45 m/s). The disk is accelerated up to a fixed speed, the flow interrupter is positioned downstream of the nozzle, and a valve between the accumulator and nozzle is opened. Shortly after the jet begins to issue from the nozzle, the high speed video camera is triggered and the flow interrupter is swung aside.

Figure A.1 Schematic of apparatus

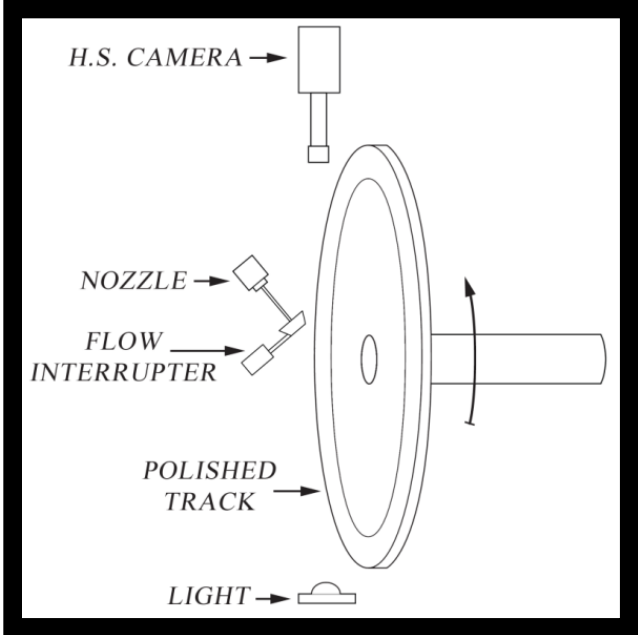
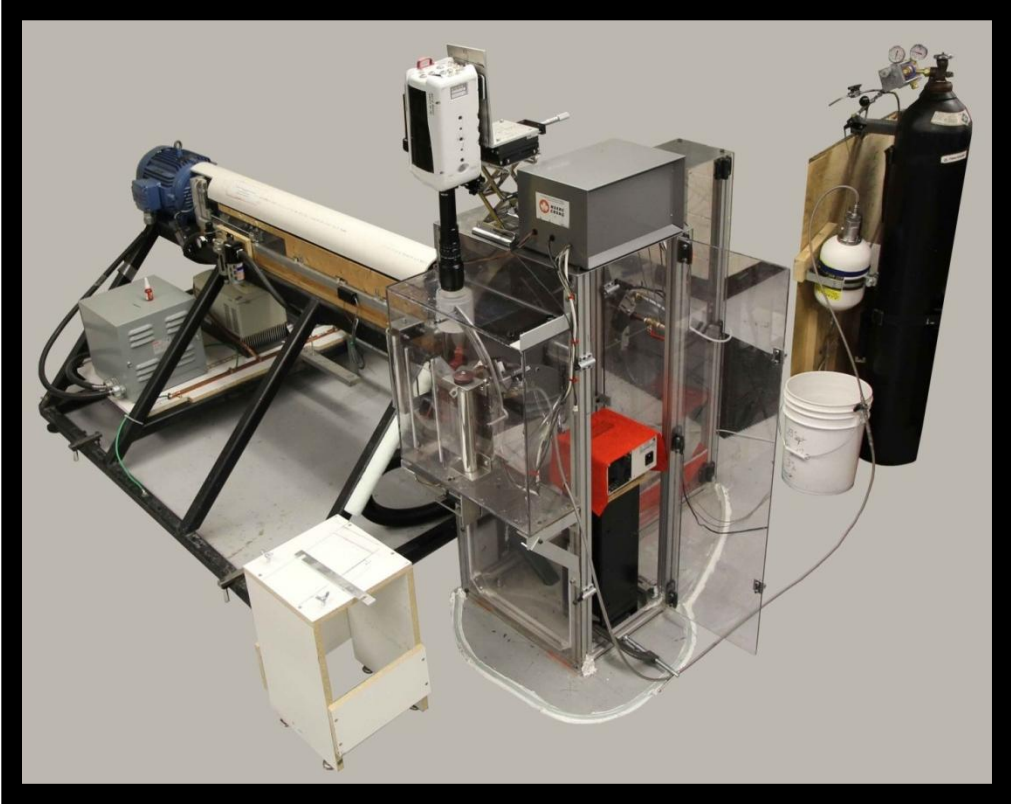


Figure A.2 Photograph of actual apparatus



A.2. The Disk

A spinning surface was designed and built specifically for providing a very high speed surface onto which a jet can impinge. To achieve the range of speeds desired (0-300km/hr), the maximum angular rate and radius of the disk needed to be high. The maximum disk radius was constrained by the size of the CNC machine intending to manufacture the disk. A radius of 12.5" (31.75cm) was chosen. Given that a motor salvaged from another experimental setup is capable of producing a maximum angular rate of 3000rpm, a total range of 0-360km/hr is achievable with the chosen motor, disk radius combination which is well above our desired speed range of 0-300km/hr. Mild, cold rolled steel was chosen for its lower manufacturing cost over stainless steel and for its ability to be polished more easily, a task which was performed by hand over an annulus whose inner radius locates 2" from the outer edge of the disk. Figure A.4 shows the reflectiveness of the surface, indicative of the quality of the polish achieved by wet-sanding the surface with progressively finer grid sandpapers (P40 to P600 grit) as the disk was spun at angular rates above 400 rpm. Following its manufacture, the disk was brought to a company, Dynamic Engineering Inc., for balancing. Figure A.3 shows the rear of the disk where material was removed to achieve the balancing of the 1/2" thick steel disk. An axle suspended by air bearing couples the shaft of the motor to the machined disk. A torque limiter is included in this coupling which prevents damage to the motor and shaft if the acceleration or deceleration of the shaft is ever to reach beyond a critical level upon which the limiter will activate and decouple the shaft from the motor until the relative velocities fall below a threshold.

Figure A.3. Balanced Disk

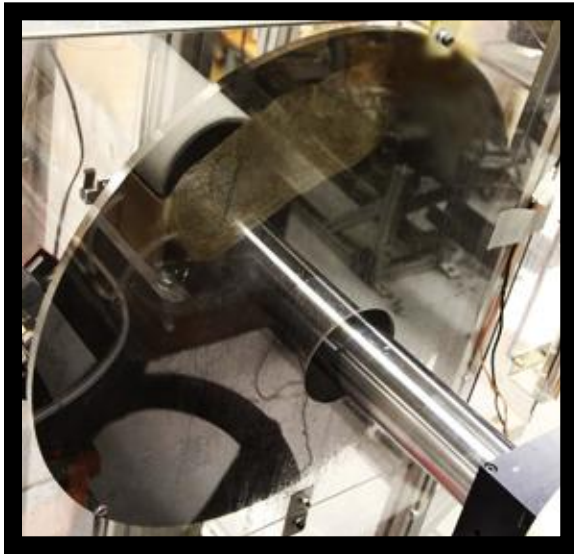


Figure A.4 Surface polish before and after buffing



A.3 Safety Enclosure

To protect users from accidentally contacting the disk while in operation and to confine all test fluids during the process of an experiment, a polycarbonate safety enclosure was designed and built with mounting places for an arc to position the nozzle assembly. Doors enabled access to the disk as well as the interior of the enclosure for servicing, adjustments, and cleaning of the viewing windows, nozzle assembly and disk. The enclosure was cleverly designed to allow for the angle of the nozzle block to be adjusted meanwhile keeping the impingement location of the jet the same, eliminating the need to refocus or reposition lighting and photographic devices. Additionally, careful thought enables two viewing angles from a camera as well as for two impingement locations, namely, on the face of the disk and on the outer edge of the disk. I and others give many thanks to Arnaud Galley (arnaud.galley@gmail.com) who

contributed his diligent and creative efforts in designing and constructing this important portion of the apparatus during his stay in Vancouver as an intern.

A.4. Nozzle Assembly

Jet stability, interchangeable nozzle sizes and variable impingement angles are facilitated by one unit. This unit consists of a nozzle block, a flow interrupter, solenoid valve, pressure transducer, and orifice holder all positioned tightly together to maintain fast response times and an accurate readout of the pressure local to the orifice. The entire assembly is fixed to an arc by a cylindrical rod, allowing the position of the orifice to be adjusted in a 2 dimensional polar coordinate system perpendicular to the impingement location. Figure A.5 and Figure A.6 respectively show the nozzle assembly affixed to the arc and an exploded view of the orifice holder. The orifice holder has been machined to conveniently accommodate precision pinhole apertures with arbitrary orifice diameters purchased from Edmund Optics. During the sequence of a test, the back pressure is first set via the auto-pressure controller, the solenoid valve is opened and the jet is made to impinge onto a collection device until the transient effects of opening the solenoid valve are dissipated. Once the nozzle back pressure reaches stability, the flow interrupter moves out of the way, the nozzle back pressure is recorded and the jet impinges on the high-speed moving surface. Figures A.8 and A.9 show optical measurements for the orifices.

Figure A.5 Nozzle block



Figure A.6 Nozzle assembly

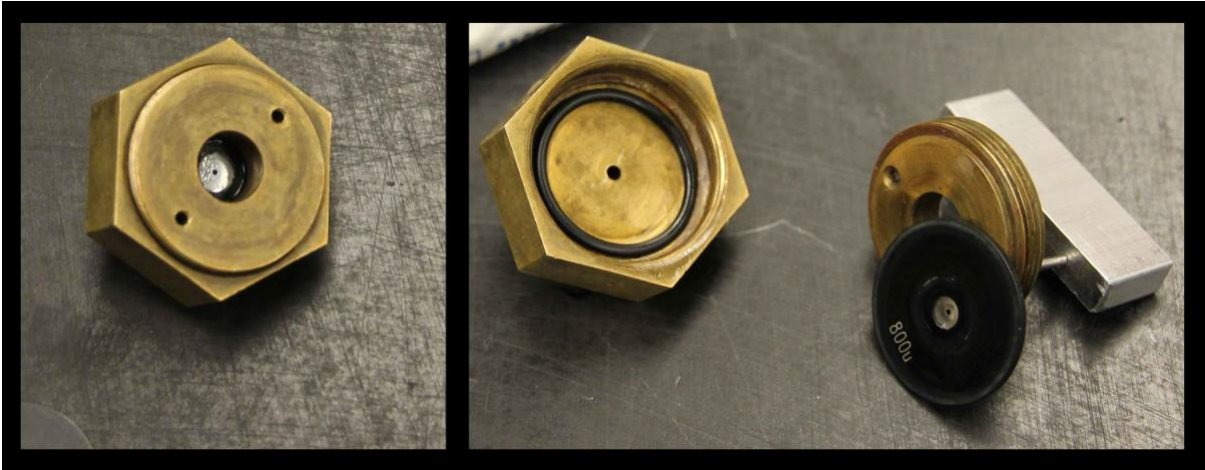


Figure A.7 Nozzle orifice pucks

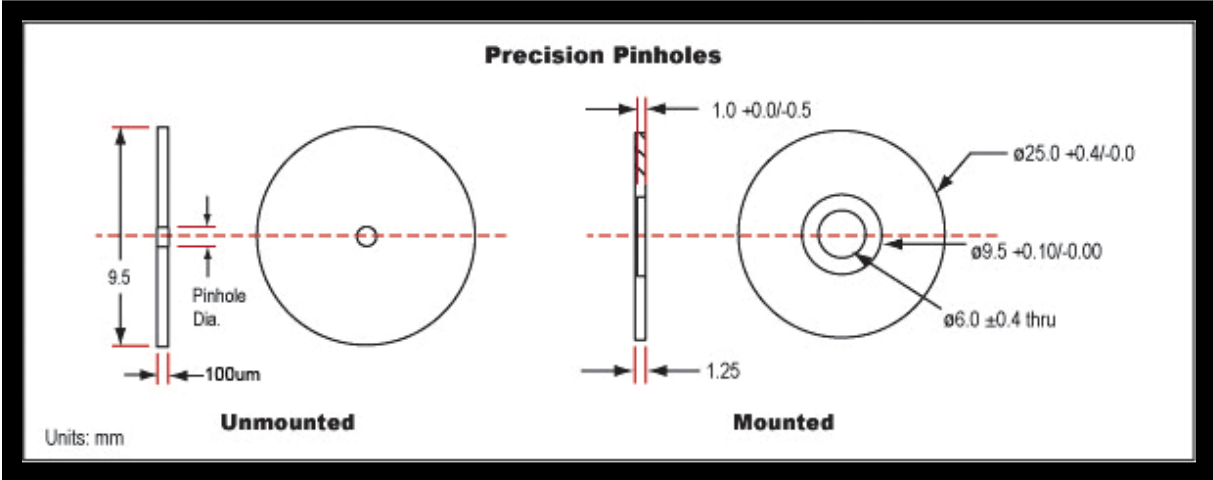


Figure A.8 Measured orifice diameters

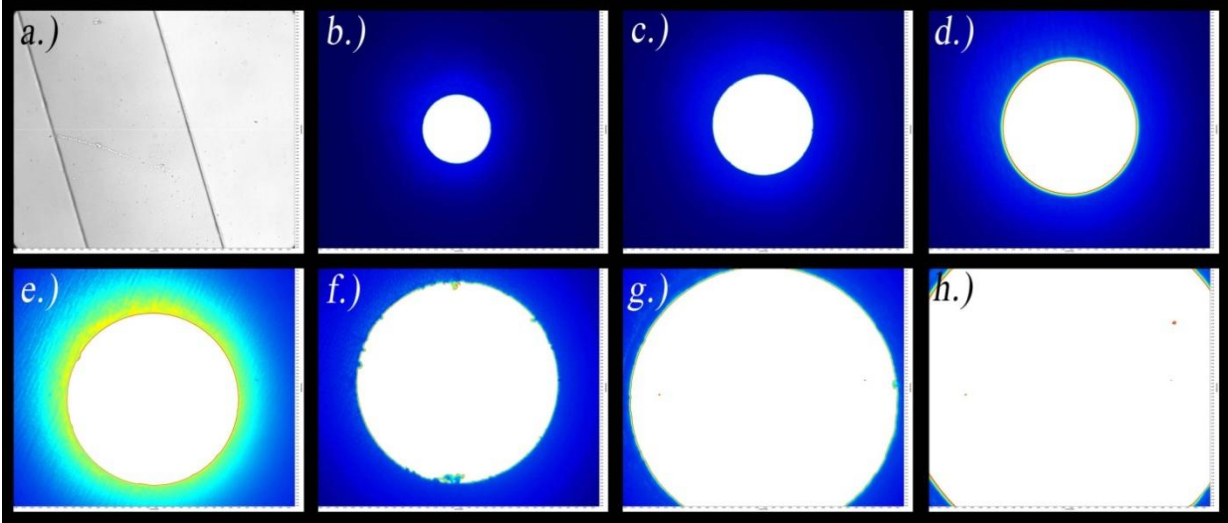
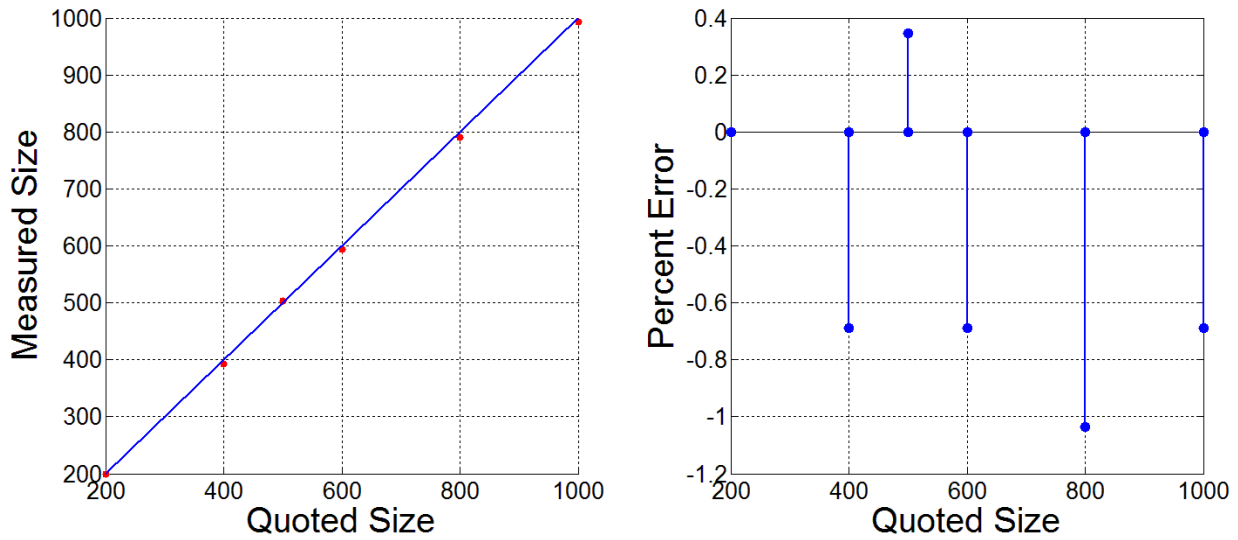


Figure A.9 Measured orifice diameters and residuals



A.5. Imaging

Imaging with two camera angles is achieved with the use of two separate lighting systems and a versatile three degree of freedom camera mount. Imaging done with the side view makes use of a high intensity fiber optic light source which can locally illuminate the impingement site without conflicting with the axle. Meanwhile imaging done with the top view makes use of a high intensity 100 watt 6700 Lumen white LED array Figure A.10 with collimating lens. The separation distance between the impingement site and the light source used for the top view is approximately 20", a factor of 5 times greater than that for the light source used in the side view. This separation distance necessitates a much higher intensity light source which is why such a bright light was chosen. For both camera angles, to protect the camera lens from fluids leaving the surface of the disk as well as to provide a clear viewing window after each test, a roll of acetate film is placed between the camera lens and a hole in the protective casing. In both cases, a phantom v611 high speed camera is used with an exposure time between 10 μ s to 50 μ s to capture video at 10,000 frames per second.

Figure A.10 High intensity LED light without collimating lens

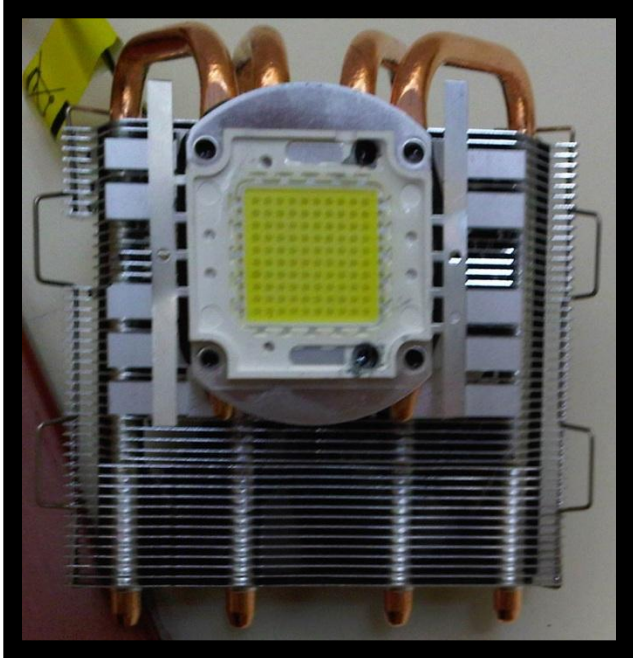
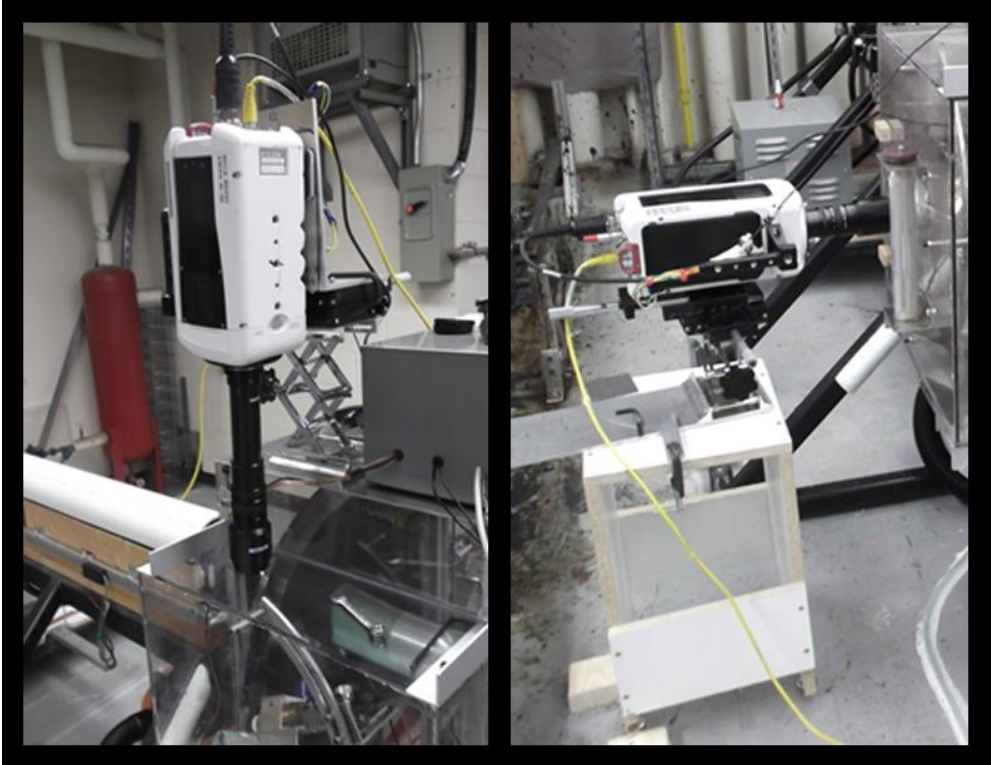


Figure A.11 Two camera angles



A.6. Auto-Pressure Controller

To ensure consistent reproduction of nozzle back pressures between subsequent tests an electronic means of regulating the back pressure was implemented. The construction involved the use of a high pressure baffle regulator, a DC, 40lb-in geared motor, a solenoid valve and needle valve used to tune the rate at which air is relieved. Feedback measurements are obtained from a high resolution pressure transducer. The DC motor is connected to an H-Bridge circuit to allow the direction to be programmatically controlled. Software was written to control the motor's duty cycle in conjunction with the relief valve's duty cycle to prevent excess loss of gasses and to increase the speed at which a targeted set-point is reached. The position of the needle valve was carefully tuned so that the maximum pressure relief rate could match the maximum rate at which the motor could reduce the pressure set-point on the baffle regulator. Two jam nuts were positioned as a safety measure to prevent pressures in excess of the capacity of the lines being produced in the unlikely event of a catastrophic failure of the control system which could tend to drive the motor continuously in a direction towards increasing pressures. This system replaces a time consuming manual method limited to accuracies of $\pm 3\text{PSI}$ with an automated method capable of producing accuracies of $\pm 0.5\text{PSI}$. Figure A.12 shows the entire assembly of all the subcomponents described above.

Figure A.12 Auto-pressure controller



A.7. Control Box

To link all the mechanical hardware to software control, a control box was built which enables low voltage, low current signals from a computer to control higher power devices. A NI USB-6009 data acquisition device (DAQ) is used to decode signals from one USB cable to control 10 digital outputs and capture pressure transducer data on one analog input. Relays whose coils driven by field effect transistors (FETs) linked to an external power supply provided the pathways for high power devices to operate upon receiving low power signals from any one of the digital outputs of the DAQ. Schematic diagrams are provided in Appendix B.

Figure A.13 Control box



A.8. Software

Lab view software offers complete operation of the experimental apparatus in two modes, namely, automatic and manual. Once opened, the front panel of Geo_Controller_V2.8.1 defaults to the automatic mode page. For user inputs, this page has two buttons and one numeric input field exist and for displays, this page has two numeric displays and a chart. The chart plots the pressure as read by the pressure transducer as a function of time while the numeric displays show the instantaneous low-pass filtered nozzle back pressure reading and the nozzle back pressure reading at the time when the camera is triggered to perform recording. Upon entering a desired set point pressure for the automated pressure regulation device, the “Set PSI” button can be pressed to initiate the transition from the current pressure to a newly desired pressure. A timer bar will appear for a total of 30 seconds and will terminate the control

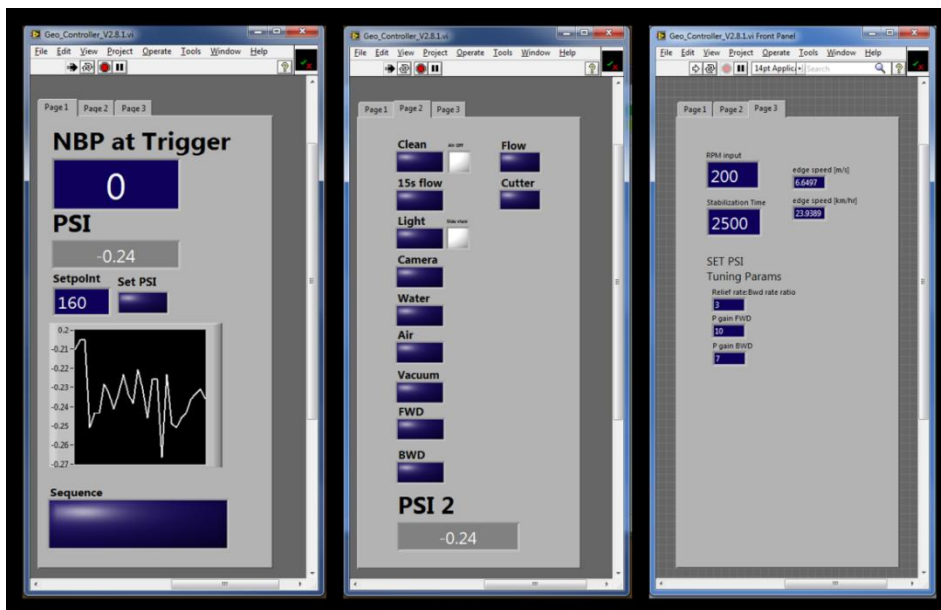
algorithm upon completion. The second button is the “Sequence” button. Once a desired back pressure is set and the user is ready to perform an impingement test, this button can be pressed to execute a sequence of commands to all the hardware necessary for performing a test. Immediately after pressing this button, the high intensity LED will activate unless it is disabled on page 2 of the front panel. A 5 second delay occurs to allow the light to stabilize in intensity. Following this, the solenoid valve on the nozzle block is activated and fluid begins to flow from the nozzle orifice onto the flow interrupter surface for a period set by the stabilization time on page 3 of the front panel. The default stabilization time is set at a conservative time of 2500ms, a time which is longer than any observed transient fluctuations of the instantaneous nozzle back pressure following the opening of the solenoid valve. This value can be lowered to conserve fluid. One can observe the pressure chart during a sequence to establish the minimum required stabilization time. Once the nozzle back pressure has stabilized, the flow interrupter is de-activated, the camera is triggered to begin recording and the jet impinges on the moving surface. Once the disk has undergone one complete revolution, the flow interrupter is again activated, preventing excess fluid from hitting the surface. Finally, a cleaning algorithm is executed which sprays water onto the surface in a sequence with pulses of compressed followed by the activation of a wet vacuum which cleans up the liquids used in the test and in cleaning.

Page 2 of the front panel allows for manual control of any single piece of hardware on the experimental apparatus as well as the execution of two sequences, namely, “15s flow” and “Clean.” “Clean” will initiate the cleaning algorithm mentioned above and the “15s flow” sequence will wait for a jet to stabilize at a given nozzle back pressure then allow the jet to spray uninterrupted for a total of 15 seconds. After 7.5 seconds the nozzle back pressure is recorded and displayed on page 1 in the numeric display labeled “NBP at Trigger.” This sequence is particularly useful when one wishes to perform mass flow rate tests. Aside from “BWD” and “FWD”, the remaining buttons have self-explanatory usages. These two buttons manually control the motor attached to the pressure regulator. It is important to avoid leaving either of these buttons active for extended periods of time as the screw the motor drives will eventually reach the end of its range and stall the DC motor, leading to potentially permanent damage to the motor windings and the driving H-bridge circuit. Most of the buttons on page 2, once pressed, will activate a timer bar

which will de-activate the button and the hardware it is controlling after an allotted time. This is to prevent the user from accidentally leaving hardware active which could invoke serious operating lifespan limitations, which are particularly true for devices such as the light, solenoid valve and flow interrupter.

Page 3 contains 5 numeric input fields and two numeric output fields. The input fields, labeled “RPM input” and “Stabilization Time” respectively determine the activation and deactivation times of the flow interrupter. While the input fields: “Relief Rate,” “P gain FWD,” and “P gain BWD” allow one to tune the control system for the automated pressure regulator. Two numeric output fields display the calculated edge speed of the disk in two different units.

Figure A.14 Control software

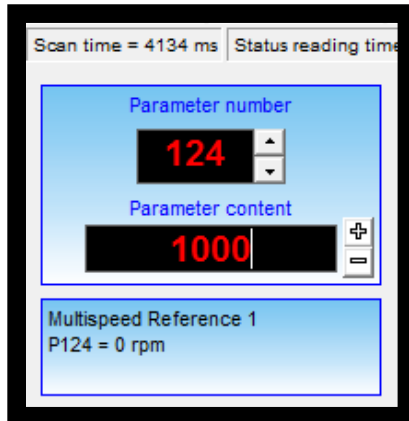


A.9. Motor Control

To control the speed of the disk using the computer, an RS232 module was purchased to interface between the computer and a variable frequency drive (VFD) motor. A software called, “SuperDrive” provides a user interface to change all parameters of the VFD. All parameters have been programmed for ideal operation including accelations and decelations profiles. The angular rate parameter is the only parameter that a user should change and is enumerated, 124. Figure A.15 shows a user entry for a

desired angular rate of 1000rpm which the disk will accelerate to following a keyboard press of the button “Enter.” After opening SuperDrive, to access the window shown in Figure A.15, Click File→Open, Click on Project2, Click Ok, Click Online→then finally Click Monitor Using Keypad. Ensure “124” is entered into the Parameter number field prior to any entries into the Parameter content field.

Figure A.15 Motor control pane



Appendix B: Schematics

Figure B.1 Relay circuits

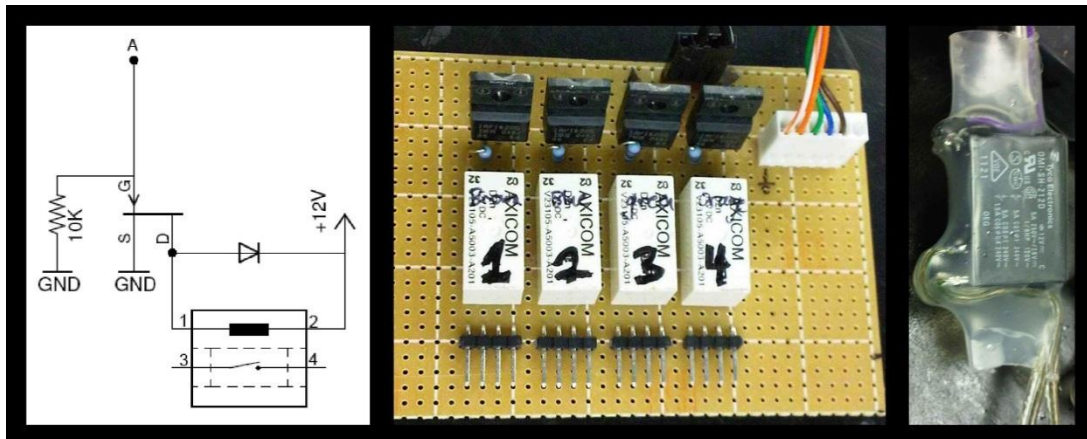
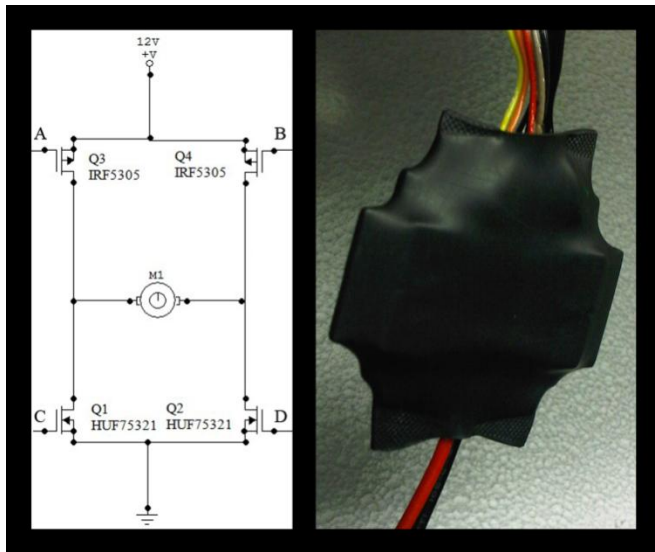


Figure B.2 H-bridge circuit



Appendix C: Supplementary Data

Figure C.1 35° water impingement results

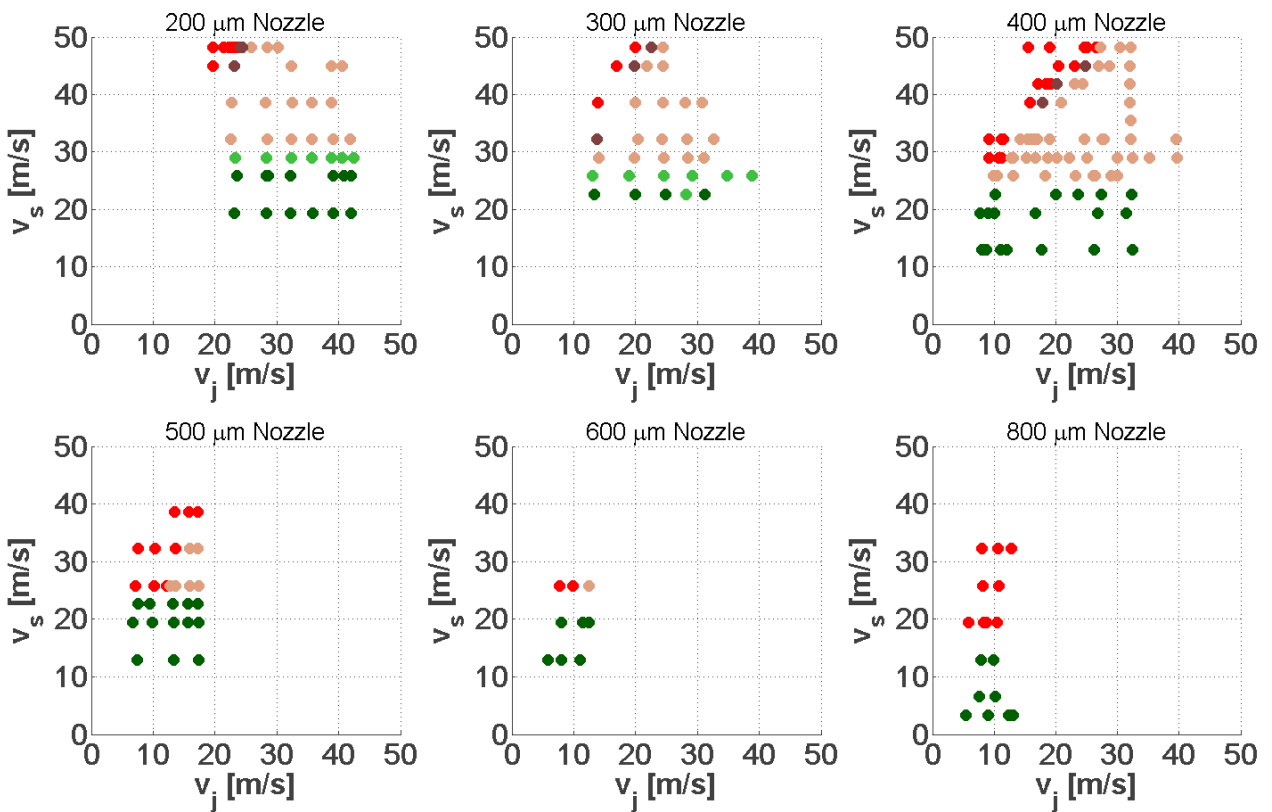


Figure C.2 60° water impingement results

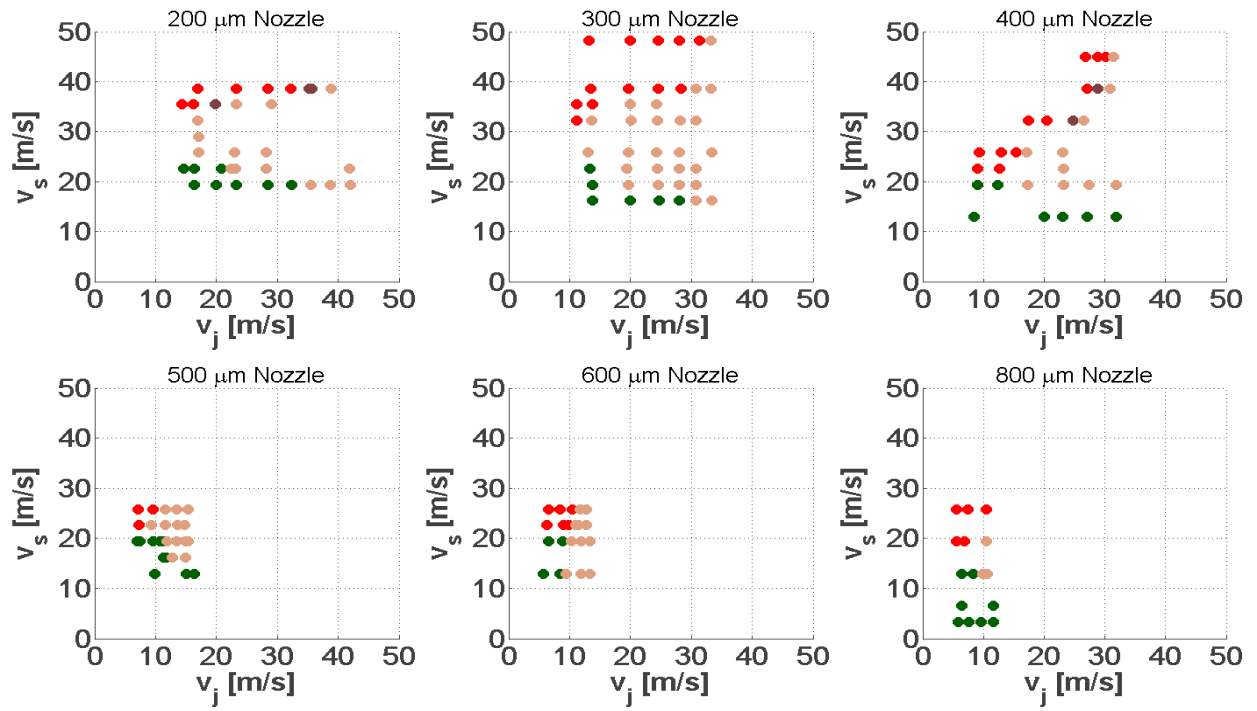


Figure C.3 90° water impingement results

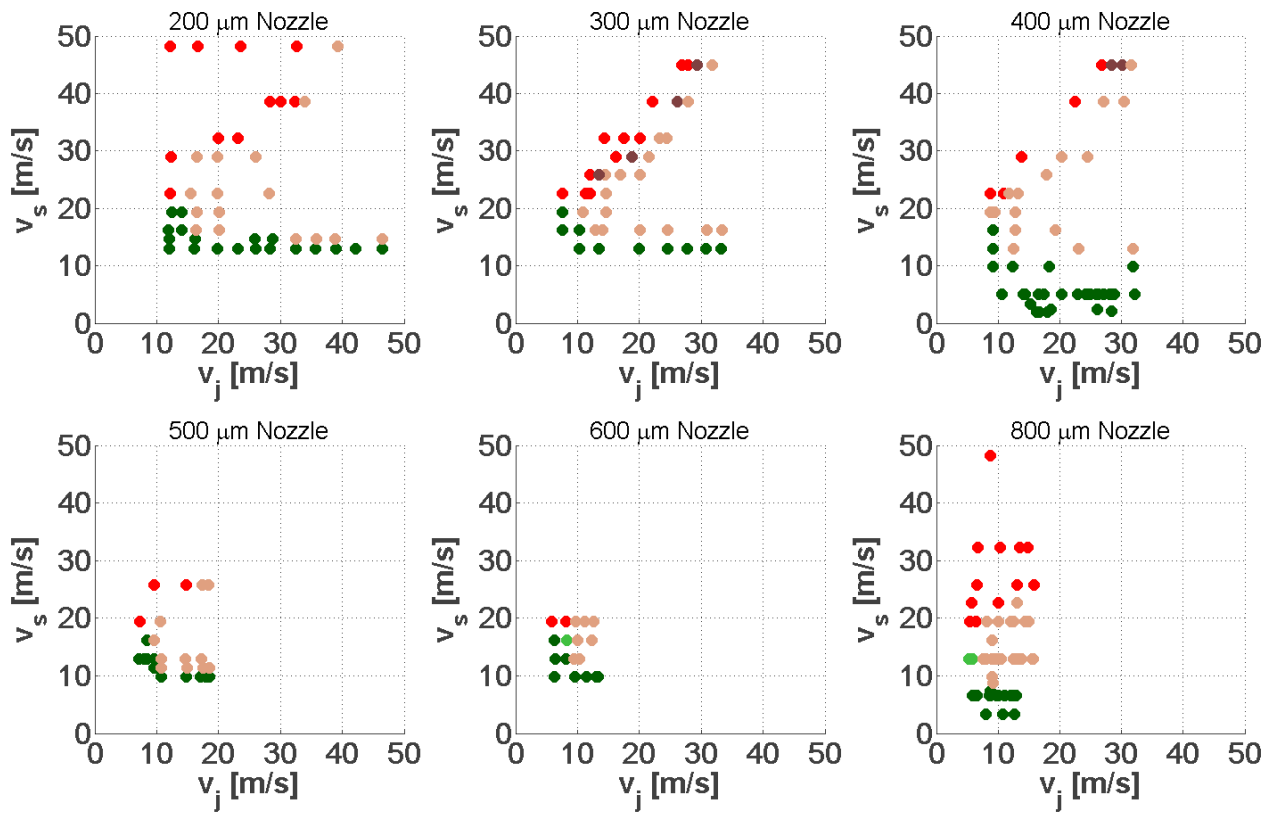


Figure C.4 135° water impingement results

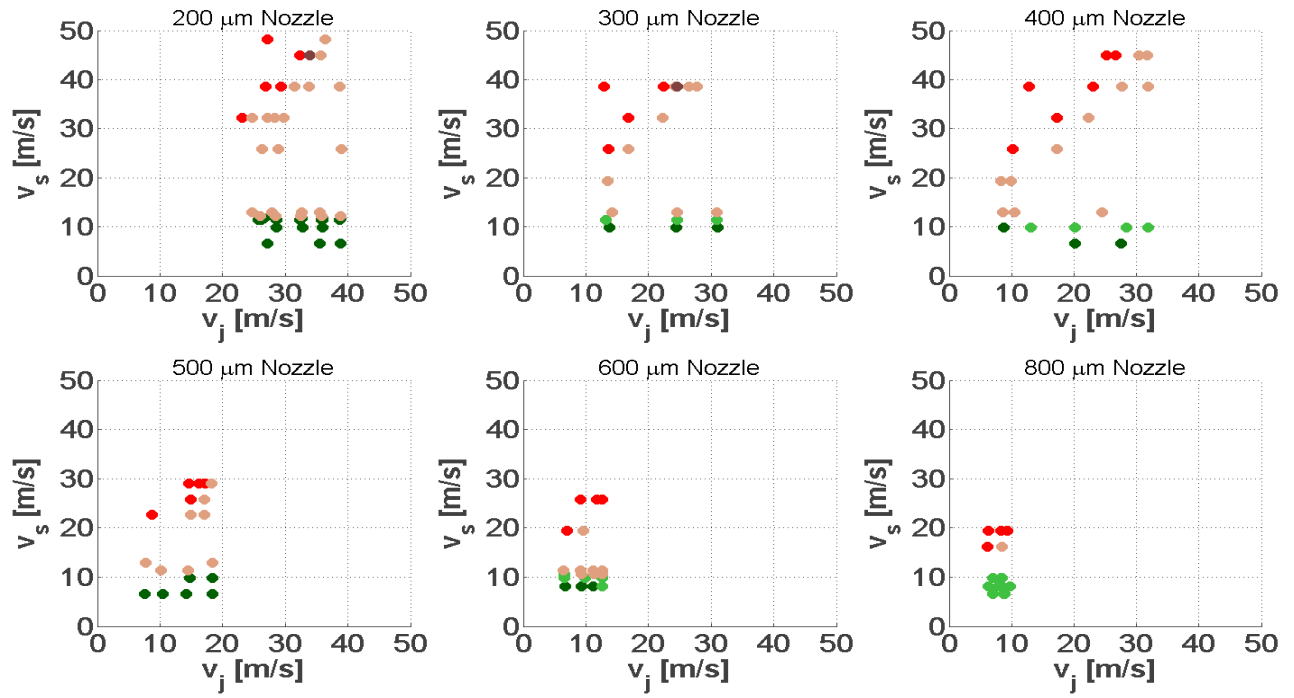


Figure C.5 160° water impingement results

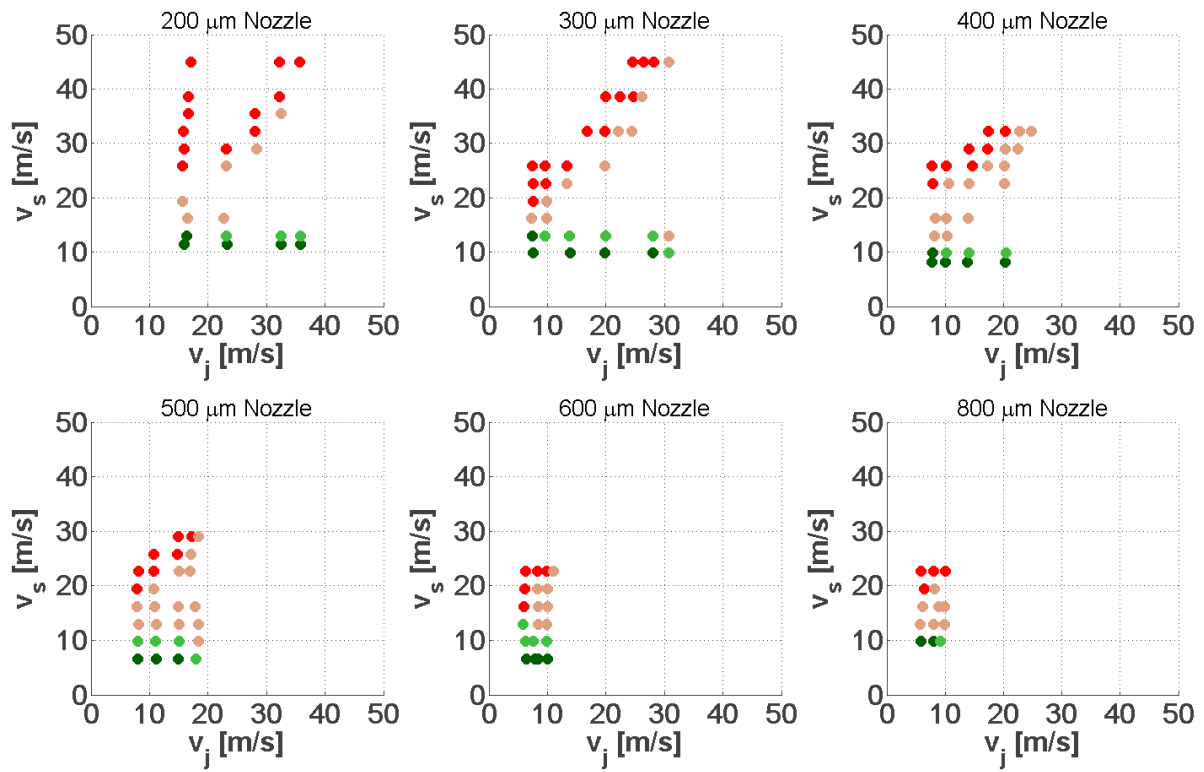


Figure C.6 73% g.w. lamella dimensions (Varied Vs, Vj)

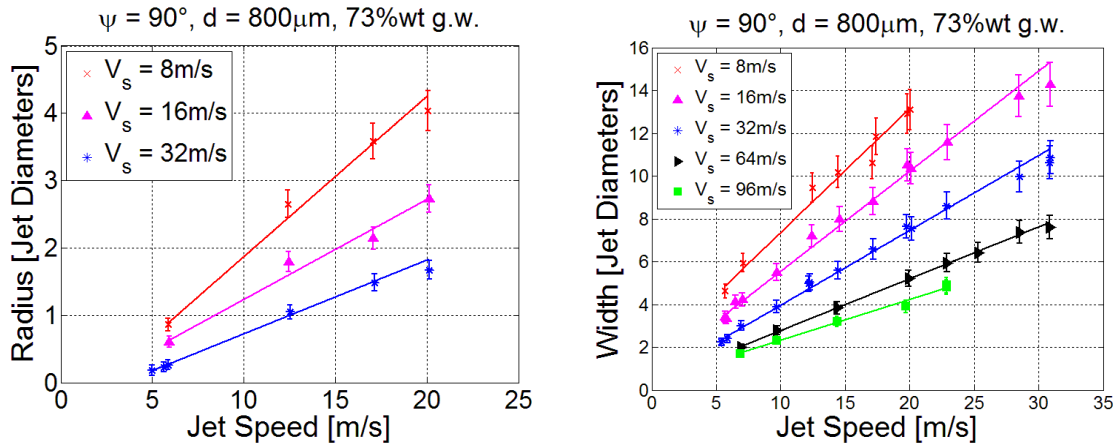


Table C.1 Fitted lines (Varied Vs, Vj)

Line: $f(V_j) = a \cdot V_j + b$	a	b	r^2
R_Vs_8	0.2381	-0.5101	0.9896
R_Vs_16	0.1485	-0.2515	0.9790
R_Vs_32	0.1096	-0.3743	0.9944
W_Vs_8	0.5797	1.5614	0.9820
W_Vs_16	0.4680	0.8670	0.9892
W_Vs_32	0.3498	0.4617	0.9926
W_Vs_64	0.2421	0.3536	0.9981
W_Vs_96	0.1900	0.4214	0.9914

Figure C.7 73% g.w. lamella dimensions (Varied d, Vj)

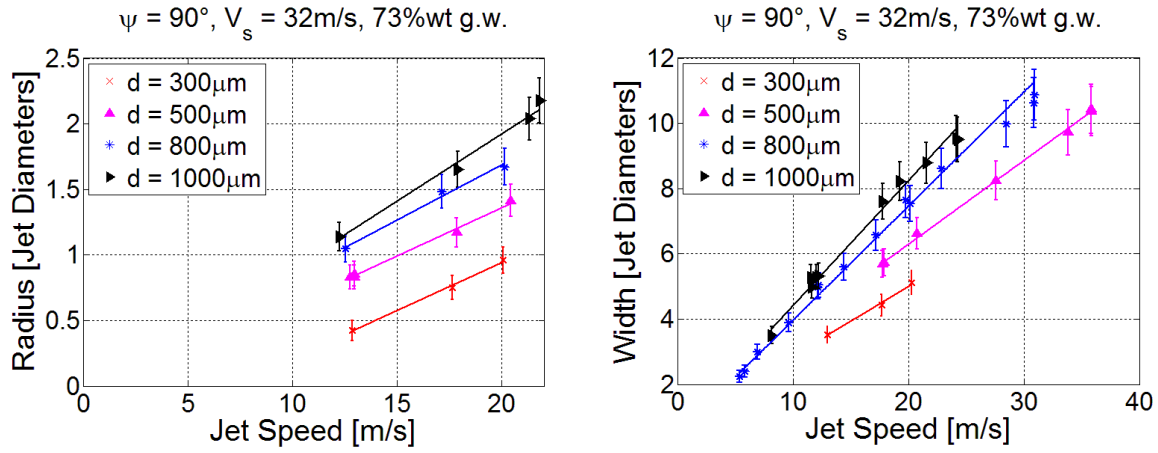


Table C.2 Fitted lines (Varied d, Vj)

Line: $f(V_j) = a \cdot V_j + b$	a	b	r^2
R_d_300	0.0731	-0.5210	0.9956
R_d_500	0.0736	-0.1132	0.9923
R_d_800	0.0843	0.0008	0.9871
R_d_1000	0.1026	-0.1285	0.9879
W_d_300	0.2124	0.7408	0.9913
W_d_500	0.2570	1.1465	0.9981
W_d_800	0.3498	0.4617	0.9926
W_d_1000	0.3836	0.5686	0.9870

Figure C.8 73% g.w. lamella dimensions (Varied ψ , V_j)

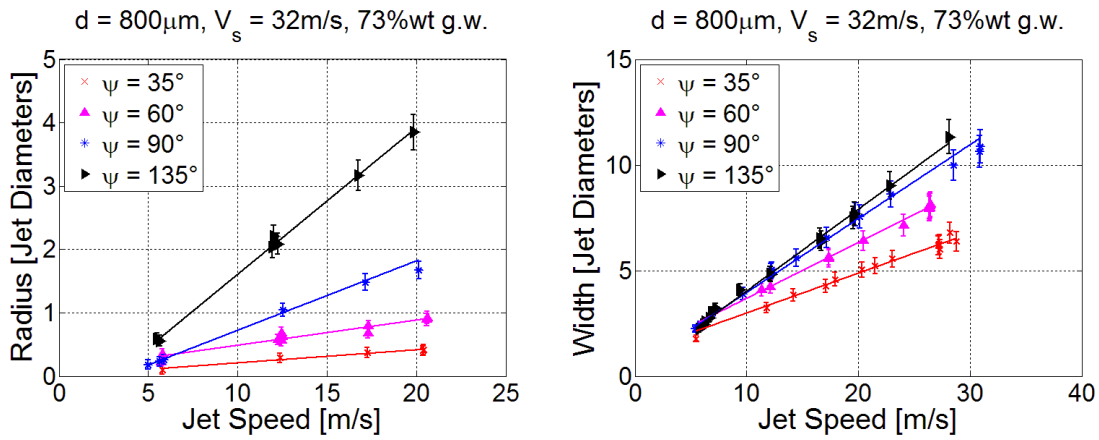


Table C.3 Fitted lines (Varied ψ , V_j)

Line: $f(V_j) = a \cdot V_j + b$	a	b	r^2
R_φ_35	0.0206	0.0000	0.9638
R_φ_60	0.0397	0.0878	0.9144
R_φ_90	0.1096	-0.3743	0.9944
R_φ_135	0.2315	-0.7077	0.9966
W_φ_35	0.1886	1.0981	0.9955
W_φ_60	0.2643	1.0379	0.9989
W_φ_90	0.3498	0.4617	0.9926
W_φ_135	0.3868	0.1602	0.9900

